

# **COULOMB IMPURITIES IN GRAPHENE QUANTUM DOTS IN A MAGNETIC FIELD**

**A Thesis Submitted to  
The Graduate School of Engineering and Sciences of  
İzmir Institute of Technology  
in Partial Fullfillment of the Requirements for the Degree of**

**MASTER OF SCIENCE**

**in Physics**

**by  
İsmail EREN**

**July 2021  
İZMİR**

## ACKNOWLEDGMENTS

Firstly, I want to thank my supervisor Prof. Dr. A. Devrim Güçlü, who helped me at difficult times, and he never put pressure on me. I have learned so much from him, and I will always appreciate his supports.

I also thank my committee members Assoc. Prof. Dr. Özgür Çakır and Assoc. Prof. Dr. A. Levent Subaşı for their evaluation of my thesis.

I am grateful to my teammates that their support and friendship. Emre Okçu and E. Bulut Kul helped me in my earliest times in the research group.

I want to thank my family for believing in me. My father, Adil Eren has always supported me, and I am grateful to be his son.

I am thankful for my soulmate Defne Yalın to be always with me and keep me motivated at all times. Words are not enough to describe her importance to me.

This work was supported by The Scientific and Technological Research Council of Turkey (TUBITAK) under the 1001 Grant Project No.119F119.

# ABSTRACT

## COULOMB IMPURITIES IN GRAPHENE QUANTUM DOTS IN A MAGNETIC FIELD

In this thesis, we investigate the atomic collapse of Graphene Quantum Dots (GQDs) in a magnetic field with the tight-binding (TB) model and mean-field Hubbard (MFH) approximation. We placed a charged impurity at the center of GQDs, and we systematically investigated the atomic collapse effect in the magnetic field by adjusting the charge of the impurity, size of the quantum dots, and magnitude of the magnetic field. It is shown that the electronic state with the lowest energy of Graphene resembled the same effect of the lowest bound state (TLBS) of atomic collapse. We confirmed the earlier findings, and we showed that the required critical charges of TLBS of the GQDs to collapse below the Fermi level are almost equal. Additionally, we investigate the formation of resonance states of GQDs, and among these resonance states, we study the evolution of the first-formed resonance state (R1). Applying a perpendicular magnetic field to GQD, decreased the critical charge of each structure, and we found that the decrease is dependent on the dot size. Moreover, we also found that TLBS of GQDs of varying sizes are crossed each other at a particular impurity charge and energy. We used the relation between the magnetic field and magnetic length ( $l_B$ ), and we compared  $l_B$  with the radius of the GQD ( $R_{GQD}$ ) in varying sizes. We found that TLBS of a GQD still converges to a particular crossing point (in terms of impurity charge and energy) as in no magnetic field when  $l_B > R_{GQD}$ . However, TLBS of a GQD diverges from the crossing point when  $l_B < R_{GQD}$ . It is studied that the continuum form of the R1 state became a chain of separated Landau levels in a magnetic field. Here we show that Landau level formation is more noticeable, and the inter-level separation of the Landau levels becomes more prominent when the  $l_B < R_{GQD}$ . Lastly, we investigated the atomic collapse of the Hofstadter's butterflies in GQDs. We found that increasing the impurity charge collapsed the energy levels. Also, increasing the impurity charge decreased (increased) the local density of states of the impurity center at the top (bottom) part of the spectrum of the Hofstadter's butterflies.

# ÖZET

## MANYETİK ALAN ALTINDAKİ GRAFEN KUANTUM NOKTALARDA COULOMB SAFSIZLIKLARI

Bu tezde, tight-binding (TB) modeli ve mean-field Hubbard (MFH) yaklaşımı ile Grafen kuantum noktalarının (GQD'ler) atomik çöküşünü manyetik alan içerisinde araştırdık. GQD'lerin merkezine yüklü bir safsızlık yerleştirdik ve safsızlığın yükünü, kuantum noktalarının boyutunu ve manyetik alanın büyüklüğünü ayarlayarak manyetik alandaki atomik çökme etkisini sistematik olarak araştırdık. Önceki çalışmalarda Grafenin en düşük enerjiye sahip elektronik durumu ile atomik çökme etkisinin en düşük bağlı durumu (TLBS) ile benzerliği gösterilmiştir. Daha önceki verileri doğrulayarak ve GQD'lerin TLBS'lerinin Fermi seviyesinin altına çökmesi için gereken kritik yüklerin neredeyse birbirlerine eşit olduğunu gösterdik. Ek olarak, GQD'lerin rezonans durumlarının inceledik ve bu rezonans durumları arasında ilk oluşan rezonans durumunun (R1) oluşumunu araştırdık. GQD'ye dikey bir manyetik alan uygulamak yapıların kritik yükünü azalttı ve azalmanın nokta boyutuna bağlı olduğunu bulduk. Ayrıca, farklı boyutlardaki GQD'lerin TLBS'lerinin belirli bir safsızlık yükü ve enerjide birbiriyle keştiğini bulduk. Manyetik alan ve manyetik uzunluk ( $l_B$ ) arasındaki ilişkiyi kullanarak  $l_B$ 'yi değişen boyutlarda ki GQD'nin yarıçapı ( $R_{GQD}$ ) ile karşılaştırdık.  $l_B > R_{GQD}$  olduğunda GQD'nin TLBS'sinin manyetik alan olmadığı durumda ki gibi hala belirli bir geçiş noktasına (safsızlık yükü ve enerji açısından) yakınsadığını bulduk. Ancak,  $l_B < R_{GQD}$  olduğunda GQD'nin TLBS'si geçiş noktasından uzaklaştığını bulduk. R1 durumunun süreklilik formunun, manyetik alan etkisinde ayrışık Landau seviyelerinin zincirlenmiş haline geldiği incelenmiştir.  $l_B < R_{GQD}$  olduğu durumda Landau seviyesi oluşumunun daha belirgin olduğunu ve Landau seviyelerinin seviyeler arası ayrımının daha belirginleştiğini gösterdik. Son olarak, GQD'lerdeki Hofstadter'in kelebeklerinin atomik çöküşünü araştırdık. Safsızlık yükünün artmasının enerji seviyelerini çökerttiğini bulduk. Ayrıca, kirlilik yükünün artırılması, Hofstadter kelebeklerinin spektrumunun üst (alt) kısmındaki kirlilik merkezinin durumlarının yerel yoğunluğunu azalttı (arttırdı).

# TABLE OF CONTENTS

LIST OF FIGURES .....	vi
LIST OF TABLES .....	viii
LIST OF ABBREVIATIONS .....	ix
CHAPTER 1. INTRODUCTION .....	1
CHAPTER 2. METHODOLOGY .....	8
2.1. Tight-Binding Model .....	8
2.2. Peierls Substitution .....	11
2.3. Atomic Collapse and Coulomb Impurity .....	13
2.4. Mean-field Hubbard Approximation .....	15
2.5. Further Details .....	21
2.5.1. Magnetic Length .....	21
2.5.1. Local Density of States of the Impurity Center .....	22
CHAPTER 3. RESULTS AND DISCUSSIONS .....	23
3.1. Charged Impurity .....	23
3.2. Effect of the External Magnetic field to Atomic Collapse .....	26
3.3. Atomic Collapse of Hofstadter's Butterfly .....	36
CHAPTER 4. CONCLUSION .....	41
REFERENCES .....	42

# LIST OF FIGURES

<u>Figure</u>		<u>Page</u>
Figure 1.1.	Illustration of 2D Graphene layers in a Graphite structure .....	1
Figure 1.2.	A plot of the bound energy of an atom with respect to the nucleus charge (Reprinted from the source: Moldovan et al. (2016)) .....	3
Figure 1.3.	Evolution of atomic collapse in Graphene at increasing charged impurity (Reprinted from the source: Wang et al. (2013)) .....	4
Figure 1.4.	The atomic collapse of GQDs with varying sizes (Reprinted from the source: Polat et al. (2020)) .....	5
Figure 1.5.	Formation of resonance states (R1, R2, R3) in Graphene for B = 0, 2, 12 T (Reprinted from the source: Moldovan (2017)) .....	6
Figure 2.1	Primitive unit vectors $\mathbf{a}_1$ , $\mathbf{a}_2$ , and $\mathbf{b}$ ; atomic sites A and B of Graphene (Remade from the source Güçlü et al. (2014)) .....	9
Figure 2.2	Depiction of atoms and bonding orbitals in Graphene .....	10
Figure 2.3	Illustration of a benzene ring in a magnetic field. Atomic sites labeled from 1 to 6 respectively .....	12
Figure 3.1	Energy of the eigenvalues vs Coupling Constant $\beta$ spectrum for a) 42, b) 546, c) 1626, and d) 5514 atoms in TB. Vertical dashed red line correspond to the location of the critical charge ( $\beta_c$ ) .....	24
Figure 3.2	Energy of the eigenvalues vs Coupling Constant $\beta$ spectrum for a) 42, b) 546, c) 1626, and d) 5514 atoms in MFH. Vertical dashed Red line correspond to the location of the critical charge ( $\beta_c$ ) .....	25
Figure 3.3	LDOS of the impurity center for a) 42, b) 546, c) 1626, and d) 5514 atoms in TB .....	25
Figure 3.4	LDOS of the impurity center for a) 42, b) 546, c) 1626, and d) 5514 atoms in MFH .....	26
Figure 3.5	LDOS of the impurity center of the 5514 atom GQD in a external magnetic field of a) 0 T, b) 10 T, c) 25T, and d) 250 T in TB .....	28
Figure 3.6	LDOS of the impurity center of the 5514 atom GQD in a external magnetic field of a) 0 T, b) 10 T, c) 25T, and d) 250 T in MFH .....	29

<u>Figure</u>	<u>Page</u>
Figure 3.7	The plot of the R1 resonance states for varying GQD for decreasing $l_B$ (increasing <b>B</b> ) in TB. Red lines referring to $l_B < R_{GQD}$ and Blue lines referring to $l_B > R_{GQD}$ . Vertical dashed red line correspond to the crossing of the TLBS. $l_B$ and $R_{GQD}$ in units of nm ..... 30
Figure 3.8	The plot of the R1 resonance states for varying GQD for decreasing $l_B$ (increasing <b>B</b> ) in TB. Red lines referring to $l_B < R_{GQD}$ and Blue lines referring to $l_B > R_{GQD}$ . Vertical dashed red line correspond to the crossing of the TLBS. $l_B$ and $R_{GQD}$ in units of nm ..... 31
Figure 3.9	The probability density of the evolution of the R1 States for 5514 atom GQD where $l_B > R_{GQD}$ ..... 33
Figure 3.10	The probability density of the evolution of the R1 States for 5514 atom GQD where $l_B < R_{GQD}$ ..... 35
Figure 3.11	The probability density of the evolution of the R1 States for 5514 atom GQD for $l_B$ is larger (a, b, c) and smaller (d, e, f) than the radius of the GQD with MFH ..... 36
Figure 3.12	Energy vs magnetic flux spectrum of Hofstadter's butterflies for the a) 366, b) 546, c) 762 atom GQDs ..... 37
Figure 3.13	LDOS of the impurity center of Hofstadter's butterflies for the a) $\beta = 0$ , b) $\beta = 0.4$ , c) $\beta = 0.8$ , and d) $\beta = 1.2$ of 5514 atom GQD in TB ..... 39
Figure 3.14	LDOS of the impurity center of Hofstadter's butterflies for the a) $\beta = 0$ , b) $\beta = 0.4$ , c) $\beta = 0.8$ , and d) $\beta = 1.2$ of 5514 atom GQD in MFH ..... 40

# LIST OF TABLES

<u>Table</u>		<u>Page</u>
Table 1.	The number of atoms, radius, and Expected Landau Level Formation according to the magnetic length formula equivalence for the considered structures .....	27

## LIST OF ABBREVIATIONS

TB .....	Tight-Binding
MFH .....	Mean-Field Hubbard
GQD .....	Graphene Quantum Dot
LDOS .....	Local Density of States
$l_B$ .....	Magnetic Length
HB .....	Hofstadter's Butterfly
TLBS .....	The Lowest Bound State
$R_{GQD}$ .....	Radius of the Graphene Quantum Dot
$\beta_c$ .....	Critical Impurity Charge
LL .....	Landau Level
CP .....	Crossing Point

# CHAPTER 1

## INTRODUCTION

Carbon is one of the most abundant elements on Earth in varying forms and sizes. From organic chemistry to the tools that we use every day, carbon exists widely with a broad range of allotropes. An allotrope of carbon is the Diamond, which has unique hardness and thermal conductivity, and is also used in semiconductors. On the other hand, another type of carbon allotrope is Graphite. Also, Graphite is frequently used in materials like; pencils, brushes to polymers and electrodes (Chung, D. D. L. (2002), Sengupta et al. (2011)). If we take a closer look at the nanostructure of graphite, it is seen that carbon atoms form honeycomb lattices layer by layer. On the other hand, layers of the graphite are bonded together by weak van der Waals forces. Even though the dynamic characteristics of the layers of graphite are subjected to investigation of intercalation in between these layers (Solin, S. A. (1982)), there are unique electronic, magnetic and optical properties in individual layers.

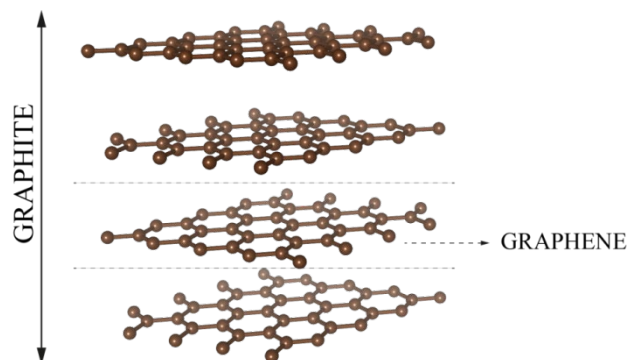


Figure 1.1. Illustration of 2D Graphene layers in a Graphite structure.

Since the first synthesis of Graphene, alternative experimental techniques, such as chemical vapor deposition and molecular beam epitaxy methods are used for growth. At the same period, the use of Graphene in applications increased exponentially. It was

shown that Graphene nanosheets are prospective anode materials for Lithium-ion Batteries (LIBs) (Yoo et al. (2008)). Also, Wang et al. studied that the Graphene nanosheets achieved unique electrochemical performance for LIBs in terms of Lithium storage and charging-discharging periods (Wang et al. (2009)). It is also noted that the potential of Graphene can be expanded with a combination of varying materials. It was proven by Su et al. that the Graphene supplemented  $\text{LiFePO}_4$  cathode shown superior performance than its bare form in energy applications (Su et al. (2010)). Additionally, Graphene is proven to be a suitable two-dimensional choice for tuning defects (Chen et al. (2017)). Another example usage of Graphene is the coating, where Graphene is shown to enhance the stability of structural integrity and functionality (Dong et al. (2018)). Also, It was studied that coating with Graphene protected against corrosion (Choi et al. (2018)).

In addition to the synthesis of Graphene, the study of carbon-based nanomaterials are subject to investigation in spintronics, flexible electronics, and all other carbon-based nanocircuits. The one-dimensional variations of carbon allotropes such as carbon nanotubes (De Volder et al. (2013)) and carbon nanoribbons (Çakmak et al. (2018)) were studied. The zero-dimensional forms of carbons are studied (Altıntaş et al., (2018); Güçlü et al. (2013); Shen et al. (2012) ).

One of the major investigated subjects on Graphene quantum dots (GQDs) is their optical properties. Ranging from photovoltaic applications to biosensors, the photoluminescent properties of GQDs are potential materials with low toxicity (Shen et al. (2012); Zheng et al. (2015)). Unique optical properties of GQDs are beneficial to photovoltaic applications and also GQDs are studied in cancer therapy investigations (Ge et al. (2014)). Similar to bulk form, GQDs took a part in the Ion battery studies. Chao et al. investigated that layering GQD on top of  $\text{VO}_2$  nanoarrays resulted in enhanced performance in Lithium-ion and Sodium-ion batteries (Chao et al. (2015)) .

It is shown that the  $p_z$  electrons near K and K' points of Graphene have a relativistic speed. The band structure of Graphene was found to be dispersed linearly, and electrons travel almost 300 slower than the speed of light in a vacuum. These properties led to Graphene obtaining massless Dirac fermions also and relativistic quantum effects have been measured (Neto et al. (2009)).

It has been assumed that an orbital of an electron on a nucleus has a stable trajectory. For a point nucleus, an electron in an orbital to fall into its nucleus can be considered as a singularity where  $r \rightarrow 0$  in a Coulomb potential. In this case, the

potential has infinite energy, and the kinetic energy should be in the same order as the potential. However, It is shown that if the nucleus is relativistic, and the charge of the nucleus becomes more than the inverse fine structure ( $\sim 137$ ), the lowest bound state (TLBS) falls into the atomic center. If the nucleus charge becomes more than the critical charge resulted in non-normalizable wavefunctions with imaginary eigenvalues.

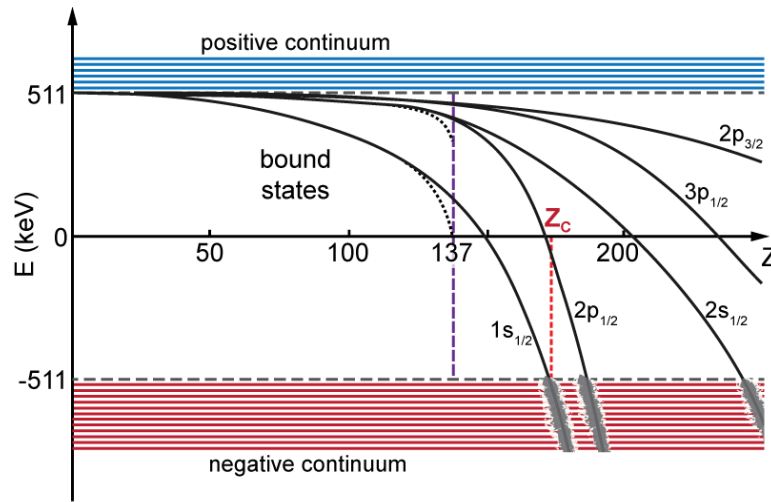


Figure 1.2. A plot of the bound energy of an atom with respect to the nucleus charge (Reprinted from the source: Moldovan et al. (2016)).

The problem can be fixed by the consideration of the finite radius of the nucleus. As seen in the Fig. 1.2., this adjustment increases the critical charge threshold of TLBS to  $\sim 172$ . After the critical point, the energy of the TLBS decreases further and interacts with the continuum spectrum of the positronic states. This interaction resulted in TLBS becoming a quasi-bound state and resonating for a finite lifetime. This physical phenomenon was called "atomic collapse" (Reinhardt et al. (1972)). However, the relativistic heavy atom requirement is a major challenge from the experimental perspective until the heavy-ion collision experiments were done (Cowan et al. (1985), Schweppe et al. (1983)).

It is shown that the electronic state with the lowest energy of Graphene in a Coulomb potential is analogous to TLBS of the atomic collapse by having the fine structure constant of Graphene is close to the Sommerfeld fine structure constant, and relativistic nature of the charge carriers. Electronic energy states of Graphene act as

TLBS, and the electron-positron pairs become to the electron-hole pairs. Moreover, the transformation of TLBS into the resonance states of the atomic collapse was shown in Graphene as the electronic state with the lowest energy becomes quasi-bound and resonating states after a certain impurity charge.

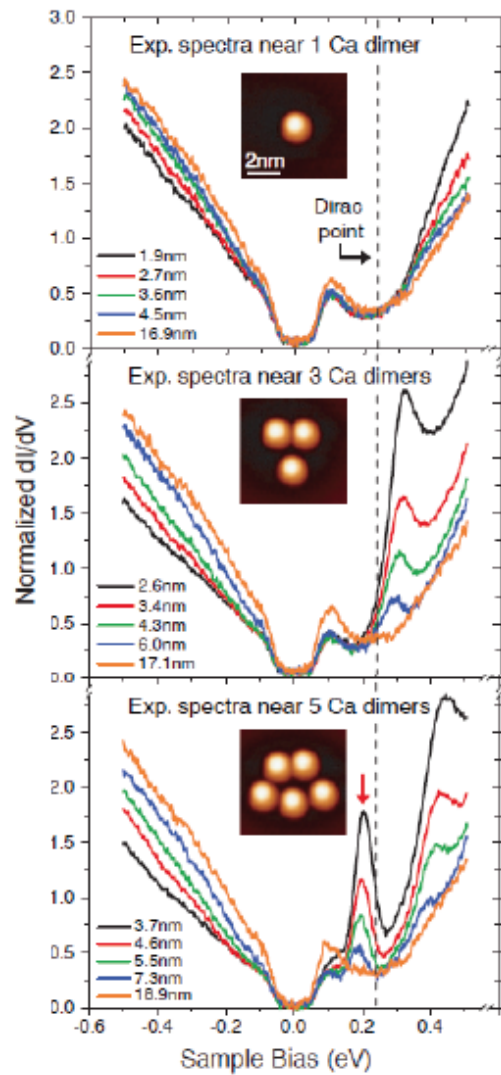


Figure 1.3. Evolution of atomic collapse in Graphene at increasing charged impurity (Reprinted from the source: Wang et al. (2013)).

As you can see in Fig. 1.3. the atomic collapse effect in Graphene observed experimentally. Wang et al. observed an analogous effect by placing Ca dimers on Graphene where the increasing number of the Ca dimers resulted that the electronic

states shifting below the Fermi-level and resulting in almost bound states (Wang et al. (2013)).

After the experimental realization of atomic collapse phenomena in Graphene, theoretical studies still continuing to investigate this subject (Kul et al. (2020)). Although Graphene modeled as an infinitely long two-dimensional material, considering it as a quantum flake at differing sizes is beneficial to revealing size effects. Polat et al. investigated the GQDs in hexagonal armchair form with varying sizes by placing a Coulomb impurity at the center of each dot as you can see in Fig. 1.4. They showed that the critical impurity charge for the lowest electronic state to cross over the Fermi level remained the same in GQDs (Polat et al. (2020)).

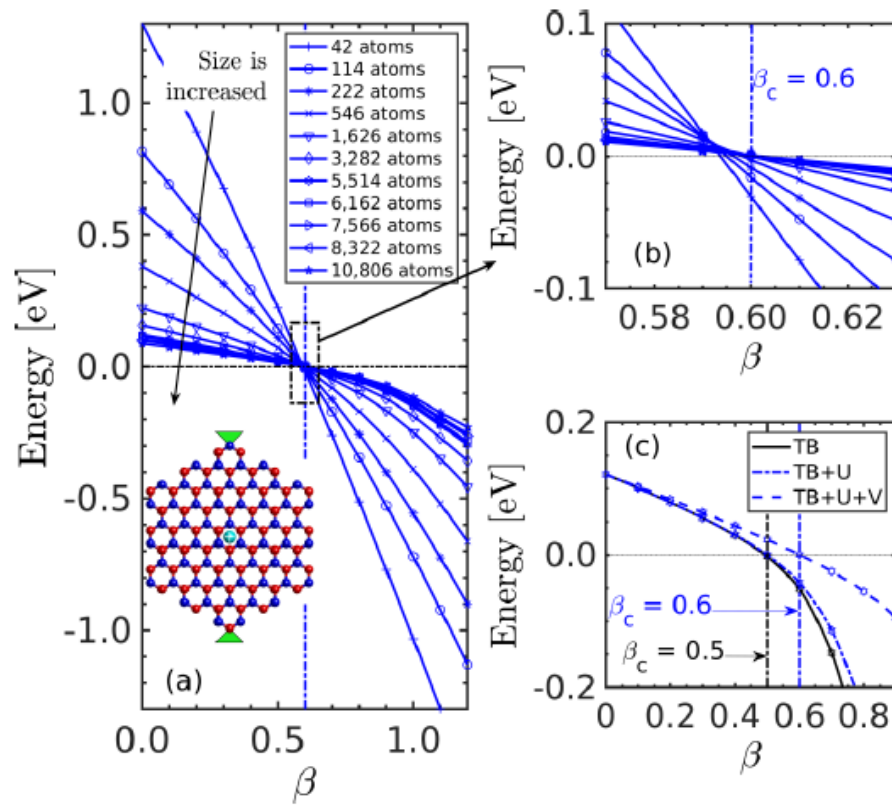


Figure 1.4. The atomic collapse of GQDs with varying sizes (Reprinted from the source: Polat et al. (2020)).

In this thesis, we accepted the findings of Polat et al. as one of our reference points. As discussed earlier, TLBS forms into a resonance state at an increasing

impurity charge. We investigate the resonance state formation of hexagonal armchair GQDs with varying sizes.

Moreover, Graphene is shown to be a unique work ground for magnetic interaction, such as the quantum Hall effect (Novoselov et al. (2007)) and Hofstadter's butterfly (Hofstadter (1976)). Similar to the atomic collapse effect, the motion of electrons can be affected by a magnetic field. Moldovan et al. studied that the magnetic field on the atomic collapse of Graphene. By adjusting the strength of the magnetic field and the charge of the impurity, they showed the influence of the magnetic field decreased the critical charge of TLBS which the energy of TLBS lower than the Fermi level. (Moldovan et al. (2017)). As seen in Fig. 1.5. that continuum form of the resonance states are noticeable with no magnetic field. Moldovan et al. showed that Landau levels became distinguishable in the energy and impurity charge spectrum by applying a small magnetic field to the Graphene. Furthermore, increasing the strength of the magnetic field, reshaped the continuum form of the resonance states into the series of Landau Levels.

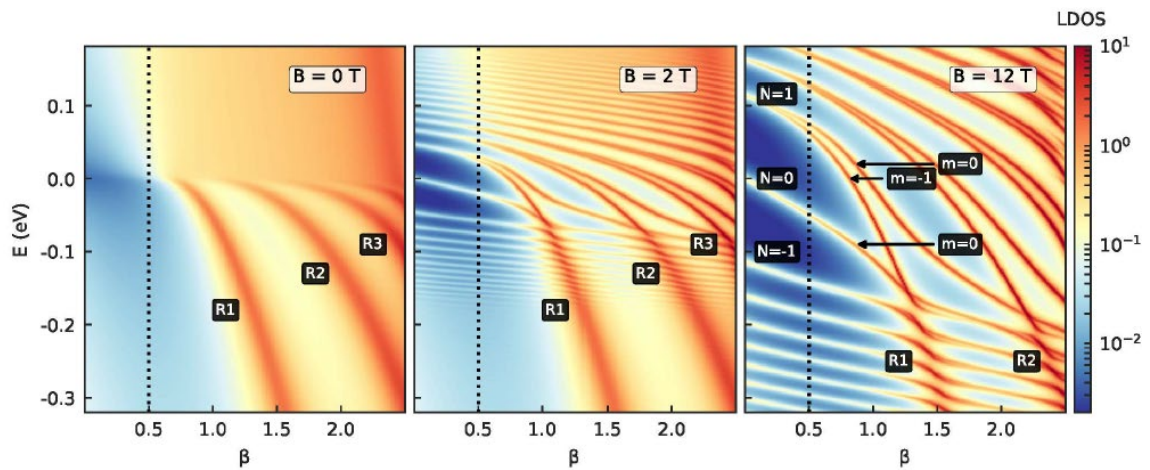


Figure 1.5. Formation of resonance states (R1, R2, R3) in Graphene for  $B = 0, 2, 12$  T (Reprinted from the source: Moldovan (2017)).

In this thesis, we investigate the atomic collapse effect in hexagonal armchair GQDs with varying sizes under a magnetic field in Tight-binding and Mean-field

Hubbard methods. We consider the first formed resonance state (R1) in terms of impurity charge where R1 originated from TLBS. We study R1 and TLBS by adjusting the quantum dot size and magnetic field strength. We compared the radius of the quantum dots with the magnetic length of the applied external magnetic field. We provided the effect of the magnetic field on TLBS and R1 state by relating to the magnetic length and the quantum dot size. Moreover, we studied the atomic collapse of the Hofstadter's butterflies of the GQDs.

## CHAPTER 2

### THEORY AND MODELS

In this chapter, we focused on the theoretical models that were used in this thesis. In order to investigate energy levels and eigenstates of the relativistic  $p_z$  electrons of the Graphene, we started with the tight-binding (TB) model (Wallace 1947). We introduced the external magnetic field perpendicular to the GQDs via the Peirels substitution (Peirels (1933), Hofstadter (1976)). To analyze the atomic collapse on GQDs, we included a Coulomb potential to an impurity. Lastly, we adopted the spin-spin interaction of  $p_z$  electron to onsite potential by the mean-field Hubbard (MFH) model (Hubbard (1963)).

#### 2.1. Tight-Binding Model

Firstly, we define structural properties of Graphene. Unit cell of Graphene consists of two Carbon atoms which are form as A and B sublattices in Hexagonal lattice. Atomic distance between two nearest Carbon atoms is  $a = 0.142$  nm. The primitive unit vectors are:

$$\mathbf{a}_1 = \frac{a}{2}(\sqrt{3}, 3), \quad \mathbf{a}_2 = \frac{a}{2}(-\sqrt{3}, 3), \quad \mathbf{b} = a(0, 1) \quad (2.01)$$

Where  $\mathbf{b}$  is defined as a vector between A and B sublattices in the same unit cell (Güçlü et al. (2014)). Using the primitive vectors, location of the A and B type atoms can be found by the following equations:

$$\begin{aligned} \mathbf{R}_A &= n\mathbf{a}_1 + m\mathbf{a}_2 + \mathbf{b} \\ \mathbf{R}_B &= n\mathbf{a}_1 + m\mathbf{a}_2 \end{aligned} \quad (2.02)$$

Above  $n$  and  $m$  are integers.

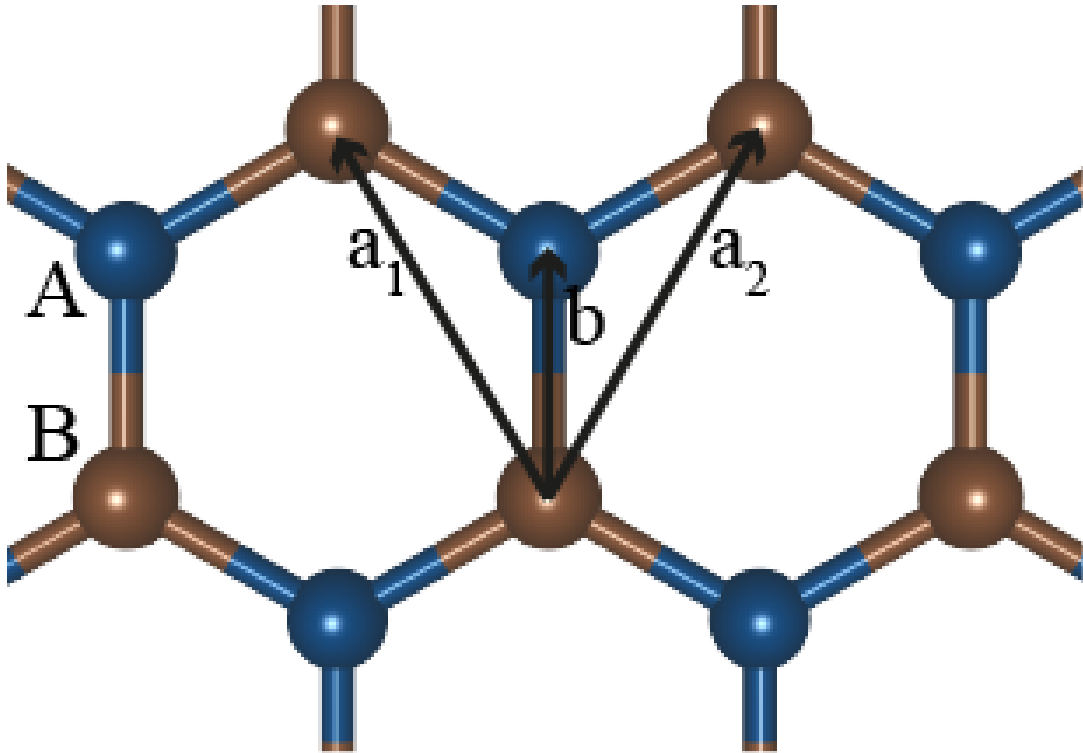


Figure 2.1. Primitive unit vectors  $\mathbf{a}_1$ ,  $\mathbf{a}_2$ , and  $\mathbf{b}$ ; atomic sites A and B of Graphene (Remade from the source Güçlü et al. (2014)).

The carbon atoms of the Graphene have four special electrons three of which contribute to  $sp^2$  hybridization. In that way, carbon atoms are tightly bonded together and give the robust character to Graphene. Meanwhile, the electron in the  $p_z$  orbital, involved in the electronic structure of Graphene by  $\pi$  bonding.

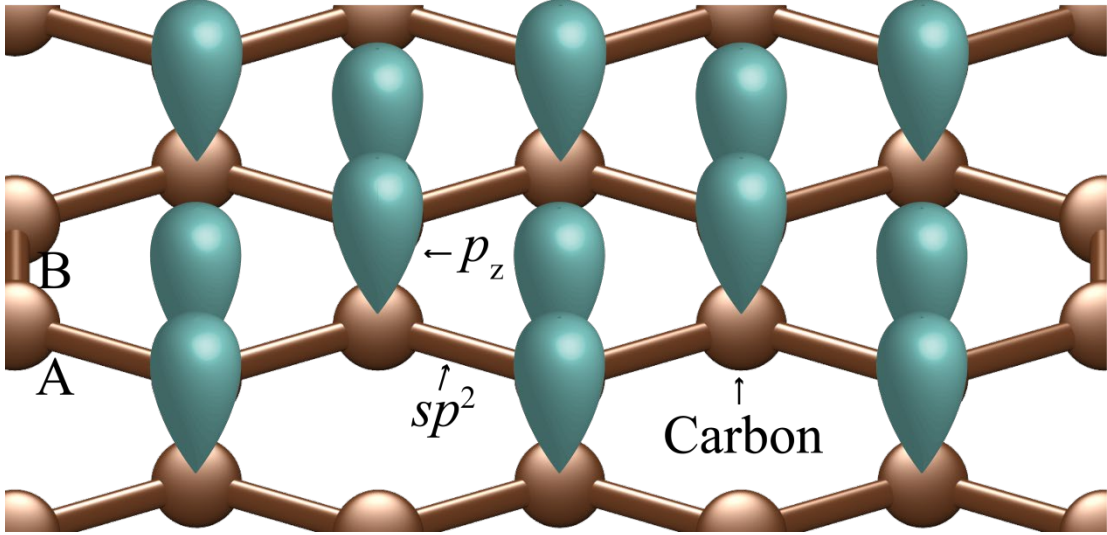


Figure 2.2. Depiction of atoms and bonding orbitals in Graphene.

Thus, before constructing our Hamiltonian, we start by defining the wavefunction of the  $p_z$  electron by using Bloch's theorem;

$$\Psi_k^A(\mathbf{r}) = \frac{1}{\sqrt{N}} \sum_{\mathbf{R}_A} e^{i\mathbf{k}\mathbf{R}_A} \phi_z(\mathbf{r} - \mathbf{R}_A), \quad \Psi_k^B(\mathbf{r}) = \frac{1}{\sqrt{N}} \sum_{\mathbf{R}_B} e^{i\mathbf{k}\mathbf{R}_B} \phi_z(\mathbf{r} - \mathbf{R}_B) \quad (2.03)$$

In the wave functions, we defined  $N$  as the number of unit cells,  $\phi_z$  is the  $p_z$  orbital, and the orbitals are orthogonal to each other. The Hamiltonian is:

$$H = \frac{p^2}{2m} + \sum_{\mathbf{R}_A} V(\mathbf{r} - \mathbf{R}_A) + \sum_{\mathbf{R}_B} V(\mathbf{r} - \mathbf{R}_B) \quad (2.04)$$

$V$  is the atomic potential at  $\mathbf{R}$ . We diagonalize the Hamiltonian as;

$$H(\mathbf{k}) = \begin{pmatrix} \langle \Psi_k^A | H | \Psi_k^A \rangle & \langle \Psi_k^A | H | \Psi_k^B \rangle \\ \langle \Psi_k^B | H | \Psi_k^A \rangle & \langle \Psi_k^B | H | \Psi_k^B \rangle \end{pmatrix} \quad (2.05)$$

We are assuming the first-nearest neighbor interactions. Thus, diagonal terms of the hamiltonian become zero.

$$\langle \Psi_k^A | H | \Psi_k^A \rangle \approx 0 \quad \langle \Psi_k^B | H | \Psi_k^B \rangle \approx 0 \quad (2.06)$$

The off-diagonal elements are;

$$\langle \Psi_k^A | H | \Psi_k^B \rangle = \frac{1}{N} \sum_{R_A, R_B} e^{ik(R_A - R_B)} \int d\mathbf{r} \phi_z^*(\mathbf{r} - \mathbf{R}_A) V(\mathbf{r} - \mathbf{R}_A) \phi_z(\mathbf{r} - \mathbf{R}_B) \quad (2.07)$$

We call the integral part of the Eq. (2.08) as hopping integral  $t$ , and its value determined experimentally that  $t \approx -2.8$  eV (Neto et al. (2009)).

$$\langle \Psi_k^A | H | \Psi_k^B \rangle = \frac{1}{N} \sum_{R_A, R_B} e^{ik(R_B - R_A)} \underbrace{\int d\mathbf{r} \phi_z^*(\mathbf{r} - \mathbf{R}_A) V(\mathbf{r} - \mathbf{R}_A) \phi_z(\mathbf{r} - \mathbf{R}_B)}_t \quad (2.08)$$

Where we considered the first nearest neighbors only. The wavevectors becomes

$$\begin{aligned} \langle \Psi_k^B | H | \Psi_k^A \rangle &= t(e^{ikb} + e^{ik(b-a_1)} + e^{ik(b-a_2)}) \\ \langle \Psi_k^A | H | \Psi_k^B \rangle &= t \underbrace{(e^{-ikb} + e^{-ik(b-a_1)} + e^{-ik(b-a_2)})}_{f(\mathbf{k})} \end{aligned} \quad (2.09)$$

Finally, we can solve the system by defining eigenvalue equation;

$$\begin{aligned} \varepsilon_{\mathbf{k}} \begin{pmatrix} c_1 \\ c_2 \end{pmatrix} &= t \begin{pmatrix} 0 & f(\mathbf{k}) \\ f^*(\mathbf{k}) & 0 \end{pmatrix} \begin{pmatrix} c_1 \\ c_2 \end{pmatrix} \\ \rightarrow \varepsilon_{\pm}(k) &= \pm t f(\mathbf{k}) \end{aligned} \quad (2.10)$$

The resulting energies are corresponding to the conduction and valence bands for positive and negative energies respectively.

## 2.2. Peierls Substitution

In this section, we introduce the perpendicular magnetic field to our solutions by implementing a vector potential  $\mathcal{A}$  associated with the magnetic field  $\mathbf{B}$ . We start with the Hamiltonian given by Eq. (2.04), under Landau Gauge transformation (Peirels (1933), Hofstadter (1976));

$$H = \frac{(\mathbf{p} - \frac{e}{c}\mathbf{A})^2}{2m} + \sum_{R_A} V(\mathbf{r} - \mathbf{R}_A) + \sum_{R_B} V(\mathbf{r} - \mathbf{R}_B) \quad (2.11)$$

Solution of the new Hamiltonian requires resulted to a phase difference to the Eq. (2.03); We can conclude that, in an applied uniform perpendicular external magnetic field, hopping parameters changed to Peierls substitution;

$$\hat{t}_{ij} \rightarrow \hat{t}_{ij} e^{i\varphi_{ij}}$$

$$\varphi_{ij} = \frac{1}{\varphi_0} \int_{r_i}^{r_j} \mathbf{A} \cdot d\mathbf{l} = \frac{B_z(x_i y_j - x_j y_i)}{2\varphi_0} \quad (2.12)$$

$$\varphi_0 = \frac{\hbar c}{e}$$

In above equation,  $\varphi_{ij}$  is the Peierls phase between  $i$  and  $j$  lattice sites.  $B_z$  is the applied magnetic field,  $x$  and  $y$  are the coordinates of corresponding axes.  $\varphi_0$  is magnetic quantum flux. The second-quantization formalizm. TB Hamiltonian becomes:

$$H_{TB} = \sum_{\langle i,j \rangle \sigma} \hat{t}_{ij} e^{i\varphi_{ij}} c_{i\sigma}^\dagger c_{j\sigma} + h.c. \quad (2.13)$$

For example, to define the Hamiltonian of a benzene ring referring to Fig. 2.3., we can construct a matrix in the following form;

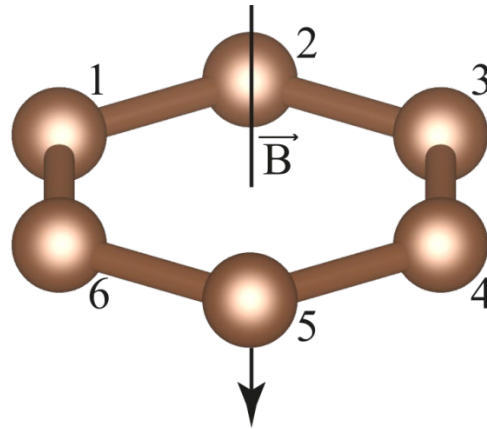


Figure 2.3. Illustration of a benzene ring in a magnetic field. Atomic sites labeled from 1 to 6 respectively.

$$H_{TB} = t \begin{pmatrix} 0 & e^{i\varphi_{12}} & 0 & 0 & 0 & e^{i\varphi_{16}} \\ e^{i\varphi_{21}} & 0 & e^{i\varphi_{23}} & 0 & 0 & 0 \\ 0 & e^{i\varphi_{32}} & 0 & e^{i\varphi_{34}} & 0 & 0 \\ 0 & 0 & e^{i\varphi_{43}} & 0 & e^{i\varphi_{45}} & 0 \\ 0 & 0 & 0 & e^{i\varphi_{54}} & 0 & e^{i\varphi_{56}} \\ e^{i\varphi_{61}} & 0 & 0 & 0 & e^{i\varphi_{65}} & 0 \end{pmatrix} \quad (2.14)$$

We can use this method for the construction of bigger GQDs with desired magnetic fields.

### 2.3. Atomic Collapse and Coulomb Impurity

The hamiltonian of a hydrogen atom in free space (Griffiths et al. (2018)) is shown by;

$$H = \frac{p^2}{2m} - \frac{1}{4\pi\epsilon_0} \frac{e^2}{r} \quad (2.15)$$

Let us consider the potential part of the Hamiltonian which we refer to as Coulomb potential. To define atoms with varying nucleus charges, the potential simplify to;

$$V(r) = -\frac{1}{4\pi\epsilon_0} \frac{e^2}{r} \rightarrow -\frac{1}{4\pi\epsilon_0} \frac{Ze^2}{r} \quad (2.16)$$

To define other atoms in free space, the potential changes to (Shytov et al. (2009));

$$\Delta p \Delta r = \hbar$$

$$K(r) = \frac{p^2}{2m} \rightarrow \frac{\hbar^2}{2mr^2} \quad (2.17)$$

Then the Hamiltonian becomes in terms of radius;

$$H = \frac{\hbar^2}{2mr^2} - \frac{1}{4\pi\epsilon_0} \frac{Ze^2}{r} \quad (2.18)$$

As you can see from Eq. (2.18) that the kinetic term prevents an electron to fall into the nucleus. Thus, quantum mechanical description requires an infinite amount of energy for  $r \rightarrow 0$ . High kinetic energy required the relativistic effect and applying relativity to the Eq. (2.17);

$$K(r) = \frac{p^2}{2m} \rightarrow c\sqrt{p^2 + m_e^2 c^2} \sim cp \rightarrow \frac{\hbar c}{r} \quad (2.19)$$

With the last result, the kinetic energy has the same order as the potential energy. Thus, we have an opening for an electron to fall into the nucleus. Dirac equation for a 1S state reveal that;

$$E_{1S_{1/2}} = m_e \sqrt{1 - \left(\frac{Ze^2}{\hbar c}\right)^2} \quad (2.20)$$

$$\frac{e^2}{\hbar c} = \alpha, \quad \alpha \approx \frac{1}{137} \quad (2.21)$$

Where  $\alpha$  is the fine structure constant. The energy of the 1S state becomes complex when the  $Z = \alpha^{-1}$ . Further revealed that electrons live up to the critical nucleus charge  $Z_c = 172$ . The region where  $137 < Z < Z_c$  is called the subcritical regime, and  $Z > 172$  is called the supercritical regime. As seen in Fig. 1.2., the electrons in the supercritical regime interacts with positronic continuum states resulted in resonance for a finite lifetime. However, these requirements bring experimental challenges. On the other hand, relativistic properties of the charge carriers in Graphene might give rise to similar physics of the atomic collapse with lesser energy (Moldovan et al. (2016)). Let consider the fine structure of the Graphene as:

$$\alpha_G = \frac{c}{v_F} \frac{\alpha}{\kappa} = 300 \frac{\alpha}{\kappa} \approx \frac{300}{137\kappa} \approx \frac{2.2}{\kappa} \quad (2.22)$$

$v_F = 10^6 \frac{m}{s}$  is the Fermi velocity, and  $\kappa \approx 2.5$  is the dielectric constant of Graphene. To describe the Coulomb potential in Graphene as close to Eq. (2.16), the

two-dimensional Dirac-Kepler problem described the electronic states in the vicinity of the impurity that radiates the Coulomb charge as (Shytov et al. (2009)):

$$\hbar v_F \begin{pmatrix} 0 & -i\partial_x - \partial_y \\ -i\partial_x + \partial_y & 0 \end{pmatrix} \Psi = \left( \varepsilon - \frac{Ze^2}{\kappa r} \right) \Psi \quad (2.23)$$

As it can be seen from the above equation that the solution depends on the Coulomb potential. We can define a new dimensionless parameter as  $\beta = Ze^2/\hbar v_F \kappa$ , where  $|\beta| < \frac{1}{2}$  is equivalent to the subcritical regime and  $|\beta| > \frac{1}{2}$  is equivalent to the supercritical regime. We will refer to  $\beta$  as coupling constant. To implement the new parameter to the Eq. (2.16), Coulomb potential can be written as:

$$V_{CP} = -\hbar v_F \beta \sum_{i,\sigma} \frac{c_{i\sigma}^\dagger c_{i\sigma}}{r_i} \quad (2.24)$$

Where we used  $r$  as the distance from impurity center to the site  $i$ . Including Eq. (2.24) to Eq. (2.14), the total Hamiltonian becomes:

$$H = \sum_{\langle i,j \rangle \sigma} (\hat{t}_{ij} e^{i2\pi\varphi_{ij}} c_{i\sigma}^\dagger c_{j\sigma} + h.c.) - \hbar v_F \beta \sum_{i,\sigma} \frac{c_{i\sigma}^\dagger c_{i\sigma}}{r_i} \quad (2.25)$$

We defined the full Hamiltonian used in the second-quantized form for the TB model.

## 2.4. Mean-field Hubbard Approximation

Additionally, we considered spin orientation of  $p_z$  electrons and onsite spin interactions by Hubbard model. To include these effects, we employed mean-field approximation to estimate ground state properties in the Hubbard model. We are starting with the full many-body Hamiltonian to define the spin-dependent potential as:

$$H = \sum_{\langle i,j \rangle \sigma} t_{ij} c_{i\sigma}^\dagger c_{j\sigma} + \frac{1}{2} \sum_{\substack{i,j,k,l \\ \sigma,\sigma', \\ \sigma'',\sigma'''}} \langle i\sigma j\sigma' | V | k\sigma'' l\sigma''' \rangle c_{i\sigma}^\dagger c_{j\sigma'}^\dagger c_{k\sigma''} c_{l\sigma'''} \quad (2.26)$$

Here, we used  $k$  and  $l$  are lattice sites,  $\sigma''$  and  $\sigma'''$  spin orientations as dummy indices for our proof.

$$\begin{aligned} \langle i\sigma j\sigma' | V | k\sigma'' l\sigma''' \rangle &= \langle ij | V | kl \rangle \langle \sigma | \sigma'' \rangle \langle \sigma' | \sigma''' \rangle \\ \langle \sigma | \sigma'' \rangle \langle \sigma' | \sigma''' \rangle &= \delta_{\sigma\sigma''} \delta_{\sigma'\sigma'''} \end{aligned} \quad (2.27)$$

$$H = \sum_{\langle i,j \rangle \sigma} t_{ij} c_{i\sigma}^\dagger c_{j\sigma} + \frac{1}{2} \sum_{\substack{i,j,k,l \\ \sigma,\sigma'}} \langle ij | V | kl \rangle c_{i\sigma}^\dagger c_{j\sigma'}^\dagger c_{k\sigma} c_{l\sigma}$$

Since we are interested in the on-site Coulomb interaction, all lattice sites are the same;  $i=j=k=l$ . The term  $\langle ij | V | kl \rangle = \langle ii | V | ii \rangle = U$ , where  $U$  is the on-site Coulomb potential.

$$\frac{1}{2} \sum_{i,j,k,l,\sigma,\sigma'} \langle ij | V | kl \rangle c_{i\sigma}^\dagger c_{j\sigma'}^\dagger c_{k\sigma} c_{l\sigma} = \frac{1}{2} U \sum_{i,\sigma,\sigma'} c_{i\sigma}^\dagger c_{i\sigma'}^\dagger c_{i\sigma} c_{i\sigma'} \quad (2.28)$$

According to Pauli-exclusion principle,  $\sigma \neq \sigma'$ . We can also define a anticommutation relation as;

$$\{c_{i\sigma} c_{i\sigma'}\} = 0 \quad c_{i\sigma'} c_{i\sigma} = -c_{i\sigma} c_{i\sigma'} \quad (2.29)$$

Using the anticommutation relation, Eq. 2.28 becomes;

$$\frac{1}{2} U \sum_{i,\sigma \neq \sigma'} c_{i\sigma}^\dagger c_{i\sigma'}^\dagger c_{i\sigma} c_{i\sigma'} = -\frac{1}{2} U \sum_{i,\sigma \neq \sigma'} c_{i\sigma}^\dagger c_{i\sigma}^\dagger c_{i\sigma} c_{i\sigma'} \quad (2.30)$$

We can also define another anticommutation relation as;

$$\{c_{i\sigma}^\dagger, c_{i\sigma}\} = 0 \quad c_{i\sigma'}^\dagger c_{i\sigma} = -c_{i\sigma} c_{i\sigma'}^\dagger \quad (2.31)$$

Using the anticommutation relation, Eq. 2.30 becomes;

$$-\frac{1}{2}U \sum_{i,\sigma \neq \sigma'} c_{i\sigma}^\dagger c_{i\sigma'}^\dagger c_{i\sigma} c_{i\sigma'} = \frac{1}{2}U \sum_{i,\sigma \neq \sigma'} c_{i\sigma}^\dagger c_{i\sigma} c_{i\sigma'}^\dagger c_{i\sigma'} \quad (2.32)$$

Next, we define the number operator as;

$$c_{i\sigma}^\dagger c_{i\sigma} = n_{i\sigma} \quad c_{i\sigma'}^\dagger c_{i\sigma'} = n_{i\sigma'} \quad (2.33)$$

Thus, the Eq. 2.32 becomes;

$$\frac{1}{2}U \sum_{i,\sigma \neq \sigma'} c_{i\sigma}^\dagger c_{i\sigma} c_{i\sigma'}^\dagger c_{i\sigma'} = \frac{1}{2}U \sum_{i,\sigma \neq \sigma'} n_{i\sigma} n_{i\sigma'} \quad (2.34)$$

For  $\sigma, \sigma'$ . The spin-configurations  $\sigma, \sigma'$  can become either  $\uparrow$  and  $\downarrow$ , or  $\downarrow$  and  $\uparrow$ , respectively. Introducing the spin-configuration to the Eq. 2.34, the exact Hubbard term is found.

$$\frac{1}{2}U \sum_{i,\sigma \neq \sigma'} n_{i\sigma} n_{i\sigma'} \rightarrow \frac{1}{2}U \sum_i (n_{i\uparrow} n_{i\downarrow} + n_{i\downarrow} n_{i\uparrow}) = U \sum_i n_{i\uparrow} n_{i\downarrow} \quad (2.35)$$

Thus, Hamiltonian including Hubbard U term becomes;

$$H = \sum_{\langle i,j \rangle \sigma} \hat{t}_{ij} c_{i\sigma}^\dagger c_{j\sigma} + U \sum_i n_{i\uparrow} n_{i\downarrow} \quad (2.36)$$

The next step is introducing mean-field approximation to the Hubbard model. We start by deriving the number operators in terms of their averages as;

$$n_{i\uparrow} = \langle n_{i\uparrow} \rangle + (n_{i\uparrow} - \langle n_{i\uparrow} \rangle) \quad n_{i\downarrow} = \langle n_{i\downarrow} \rangle + (n_{i\downarrow} - \langle n_{i\downarrow} \rangle) \quad (2.37)$$

Where;

$$\Delta n_{i\uparrow} = (n_{i\uparrow} - \langle n_{i\uparrow} \rangle) \quad \Delta n_{i\downarrow} = (n_{i\downarrow} - \langle n_{i\downarrow} \rangle) \quad (2.38)$$

Then the product of the number operators with opposite spins becomes;

$$\begin{aligned} n_{i\uparrow} n_{i\downarrow} &= [\langle n_{i\uparrow} \rangle + \Delta n_{i\uparrow}] [\langle n_{i\downarrow} \rangle + \Delta n_{i\downarrow}] \\ &= \langle n_{i\uparrow} \rangle \langle n_{i\downarrow} \rangle + \langle n_{i\uparrow} \rangle \Delta n_{i\downarrow} + \langle n_{i\downarrow} \rangle \Delta n_{i\uparrow} + \Delta n_{i\uparrow} \Delta n_{i\downarrow} \end{aligned}$$

$$\Delta n_{i\uparrow} \Delta n_{i\downarrow} \approx 0$$

(2.39)

$$\begin{aligned} n_{i\uparrow} n_{i\downarrow} &= \langle n_{i\uparrow} \rangle \langle n_{i\downarrow} \rangle + \langle n_{i\uparrow} \rangle \Delta n_{i\downarrow} + \langle n_{i\downarrow} \rangle \Delta n_{i\uparrow} \\ &= \langle n_{i\uparrow} \rangle \langle n_{i\downarrow} \rangle + \langle n_{i\uparrow} \rangle (n_{i\downarrow} - \langle n_{i\downarrow} \rangle) + \langle n_{i\downarrow} \rangle (n_{i\uparrow} - \langle n_{i\uparrow} \rangle) \\ &= \langle n_{i\uparrow} \rangle \langle n_{i\downarrow} \rangle + \langle n_{i\uparrow} \rangle n_{i\downarrow} + \langle n_{i\downarrow} \rangle n_{i\uparrow} - \langle n_{i\uparrow} \rangle \langle n_{i\downarrow} \rangle - \langle n_{i\downarrow} \rangle \langle n_{i\uparrow} \rangle \\ n_{i\uparrow} n_{i\downarrow} &= \langle n_{i\uparrow} \rangle n_{i\downarrow} + \langle n_{i\downarrow} \rangle n_{i\uparrow} - \langle n_{i\uparrow} \rangle \langle n_{i\downarrow} \rangle \end{aligned}$$

The Hamiltonian of mean-field Hubbard becomes;

$$H_{MFH} = \sum_{\langle i,j \rangle \sigma} \hat{t}_{ij} c_{i\sigma}^\dagger c_{j\sigma} + U \sum_i (\langle n_{i\uparrow} \rangle n_{i\downarrow} + \langle n_{i\downarrow} \rangle n_{i\uparrow} - \langle n_{i\uparrow} \rangle \langle n_{i\downarrow} \rangle) \quad (2.40)$$

Our result quadratic in terms of  $c_{i\sigma}^\dagger c_{i\sigma}$ , we can proceed by including the Hamiltonians of the bulk form;

$$H_{MFH} = \sum_{i,j,\sigma} \hat{t}_{ij} c_{i\sigma}^\dagger c_{j\sigma} \rightarrow H_{MFH}^B = \sum_{i,j,\sigma} \hat{t}_{ij} c_{i\sigma}^\dagger c_{j\sigma} \quad (2.41)$$

Where  $\hat{t}_{ij}$  is the hopping parameter of the bulk Graphene. Assuming the spin-dependent number operators for pristine bulk Graphene;

$$\langle n_{i\uparrow} \rangle = \langle n_{i\downarrow} \rangle = \frac{1}{2} \quad (2.42)$$

Evaluating the MFH Hamiltonian for a general system;

$$\begin{aligned} H_{MFH} &= H_{MFH} - H_{MFH}^B + H_{MFH}^B \\ &= \sum_{\langle i,j \rangle \sigma} \hat{t}_{ij} c_{i\sigma}^\dagger c_{j\sigma} + U \sum_i (\langle n_{i\uparrow} \rangle n_{i\downarrow} + \langle n_{i\downarrow} \rangle n_{i\uparrow} - \langle n_{i\uparrow} \rangle \langle n_{i\downarrow} \rangle) \\ &\quad - \sum_{\langle i,j \rangle \sigma} \hat{t}_{ij} c_{i\sigma}^\dagger c_{j\sigma} + \frac{U}{2} \sum_i \left( n_{i\downarrow} + n_{i\uparrow} - \frac{1}{4} \right) + \sum_{i,j,\sigma} \hat{t}_{ij} c_{i\sigma}^\dagger c_{j\sigma} \end{aligned} \quad (2.43)$$

Then we get the final form of the MFH Hamiltonian;

$$H_{MFH} = \sum_{i,j,\sigma} \hat{t}_{ij} c_{i\sigma}^\dagger c_{j\sigma} + U \sum_i \left( \langle n_{i\uparrow} \rangle - \frac{1}{2} \right) n_{i\downarrow} + \left( \langle n_{i\downarrow} \rangle - \frac{1}{2} \right) n_{i\uparrow} \quad (2.44)$$

$U$  is the constant term for adding extra electron on site  $i$ , where  $U = \frac{16.522}{\kappa'} \text{ eV}$ , and  $\kappa' = 6$  is the effective dielectric constant (Güçlü (2014)). Total Hamiltonian including onsite spin interaction is:

$$H = \sum_{\langle i,j \rangle \sigma} \hat{t}_{ij} e^{i2\pi\phi_{ij}} c_{i\sigma}^\dagger c_{j\sigma} - \hbar v_F \beta \sum_{i,\sigma} \frac{c_{i\sigma}^\dagger c_{i\sigma}}{r_i} + U \sum_{i,\sigma} \left( \langle n_{i\sigma} \rangle - \frac{1}{2} \right) n_{i\sigma} \quad (2.45)$$

This how can be used for a finite size Graphene with impurities

## 2.5. Further Details

### 2.5.1. Magnetic Length

In our calculations, we consider the magnetic length for the motion of a charged particle under a magnetic field for comparison to charged impurity problem. Starting with the centripetal Newtonian force and Lorentz force;

$$\frac{mv^2}{r} = qvB \quad (2.46)$$

Where  $q = e/c$ . Solving the equation for  $r$  gives;

$$\frac{mvc}{eB} = r \quad (2.47)$$

The Eq. (2.47) is called the Larmor radius. Let consider the allowed minimum distance; according to the uncertainty principle;

$$\Delta x \Delta p \geq \frac{\hbar}{2} \quad (2.48)$$

Let assume that we are leaving the constant numbers out. Momentum can be defined as  $\Delta p = mv$ , and  $\Delta x = r$ . Replacing and solving for the momentum in the Eq. (2.48);

$$mv = \frac{\hbar}{r} \quad (2.49)$$

Applying the Eq. (2.49) to the Larmor radius formula, and solving for radius, we get;

$$\sqrt{\frac{\hbar c}{eB}} = l_B \quad (2.50)$$

The  $l_B$  is called as the magnetic length. We can simplify further by making  $\sqrt{\hbar c/e}$  equal to 26 nm. In our work,  $l_B$  is an important length scale that will be compared to the size of the QDs.

## 2.5.2. Local Density of States of the Impurity Center

Starting with the LDOS as (Polat et al. (2020)):

$$N(E, r) = \sum_n |\Psi_n(r)|^2 \delta(E - E_n) \quad (2.51)$$

Where  $\Psi$  is the eigenvector, and  $E_n$  is the eigenvalue of the n'th state. To define the LDOS of the impurity center, we used the average of the probability densities of the 6 central carbon atoms around the charge impurity;

$$|\Psi_n(r)|^2 = \frac{1}{6} \sum_i^6 |\Psi_{ni}(r)|^2 \quad (2.52)$$

LDOS will help us to monitor the evolution of the atomic collapse effect on the energy levels and the R1 state. In the work of Moldovan et al., it was indicated that LDOS becomes maximum at the impurity center. Additionally, the resonance states are experimentally detectable by measuring LDOS with scanning tunneling spectroscopy (Moldovan et al. (2017)).

## CHAPTER 3

### RESULTS AND DISCUSSIONS

In this section, we studied varying-sized armchair-edged hexagonal GQDs with tuning both external magnetic field and impurity charge to understand the atomic collapse in magnetic field. The number of atoms in the considered GQDs are 42, 114, 222, 546, 1626, 3282, 5514, 6162, 7566, 8322, and 10806 to obtain consistent system to work of Polat et al. We placed a charged impurity at the center of each structure. To identify the evolution of TLBS and R1 state of atomic collapse, the charge is adjusted in each calculation. Since we are considering only the R1 state, we acknowledged the spectrum used by Polat et al. (Polat et al. (2020)). After we found parallel results to the earlier findings, we implemented the magnetic field. We considered the case where the magnetic fields are 0, 10, 25, 50, 100, 150, 200, 250 T and compared to the radius of the structures in terms of the magnetic length. We also evaluated the probability density evolution of the R1 state in the impurity center. Finally, we investigated the atomic collapse of Hofstadter's butterflies of GQDs.

#### 3.1. Charged Impurity

We firstly started with the consideration of impurity charge without magnetic field. We tested pristine GQDs with varying sizes where the number of the atom and radius of the flakes are differ in each structure. Primary calculations are done in TB and the results can be seen in Fig. 3.1.

Atomic collapse calculations of GQDs from small to bigger in terms of radius are presented in Fig. 3.1. It is noticeable that energy levels are affected by the impurity charge independent from the dot size. As the size of the GQD increases, energy levels close to the Fermi level in terms of eigenvalue energy, converged to the Fermi level.

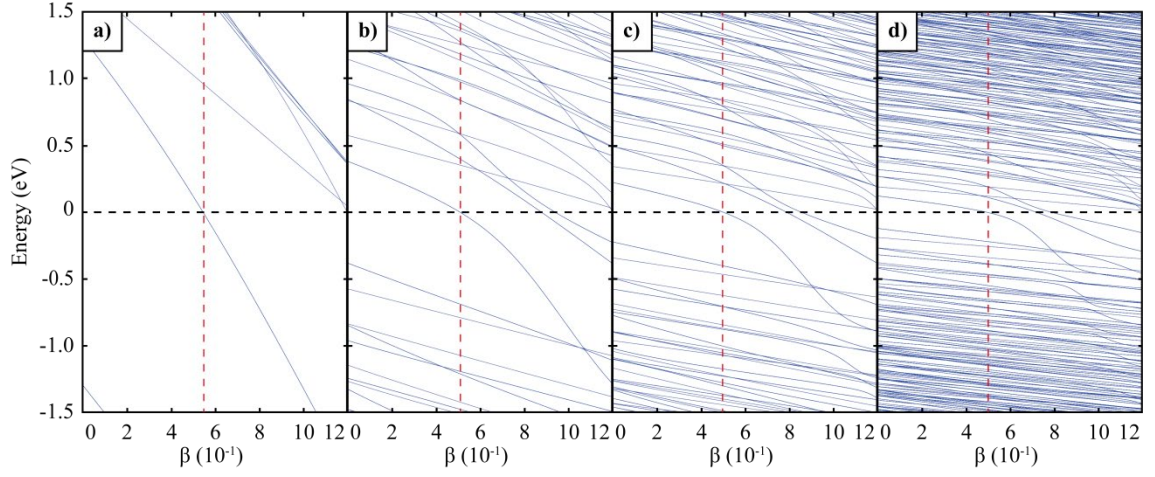


Figure 3.1. Energy of the eigenvalues vs Coupling Constant  $\beta$  spectrum for a) 42, b) 546, c) 1626, and d) 5514 atoms in TB. Vertical dashed red line correspond to the location of the critical charge ( $\beta_c$ ).

It is shown by Polat et al. that independent of the size of the GQD, TLBSs cross the Fermi Level at the same point. As seen in both Figs. 3.1. and 3.2. that atomic collapse affected the whole spectrum with including TLBS. Introducing the MFH to the TB slightly changed the  $\beta_c$ , but the atomic collapse effect was seen in both methods. Additionally, our study is consistent with the work of Polat et al. in TB and MFH formalism without a magnetic field.

We took our starting point referring to both of the results of Polat et al. and Moldovan et al. Indicated by the Moldovan et al., atomic collapse can be observable in the resonance states of the LDOS of the charged impurity center. It has been noted that scanning tunneling spectroscopy is experimental instrumentation that observes the LDOS. Also, the LDOS becomes maximum at the impurity center. In short, resonance states are measured by experimental techniques by observing the LDOS at the impurity center. We considered the LDOS of the impurity center based on the eigenvalues and eigenfunctions of the GQDs. We contour plotted the LDOS on top of the spectrum of energy and coupling constant, and it can be seen for TB in Fig. 3.3.

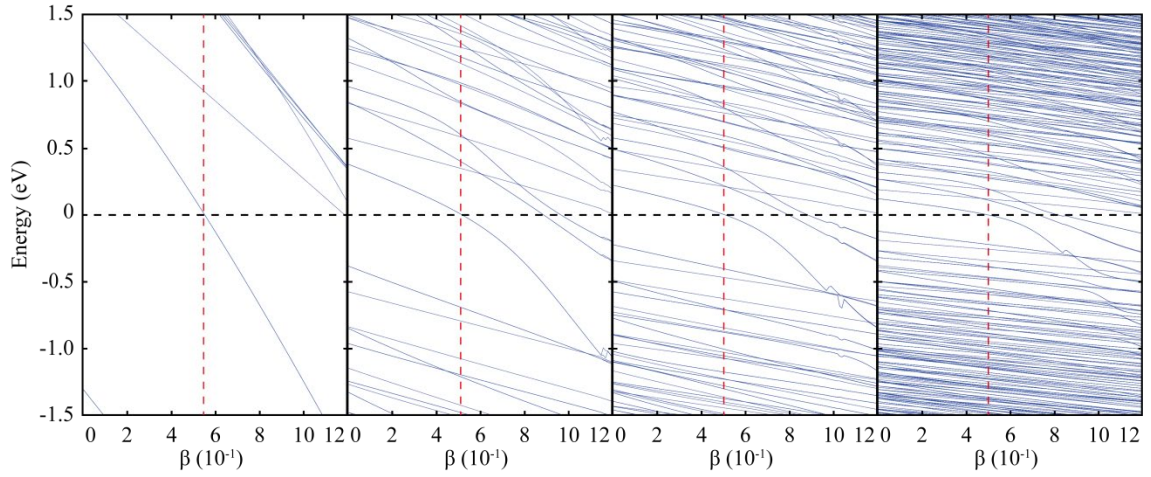


Figure 3.2. Energy vs Coupling Constant spectrum for a) 42, b) 546, c) 1626, and d) 5514 atoms in MFH. Vertical dashed red line correspond to the location of the  $\beta_c$ .

As it can be seen from Fig. 1.5. that resonance states become more prominent at the regime where the impurity charge greater than the  $\beta_c$  (supercritical). In this thesis, we concerned about the first resonance state (R1) which requires relatively lower impurity charge than other resonance states.

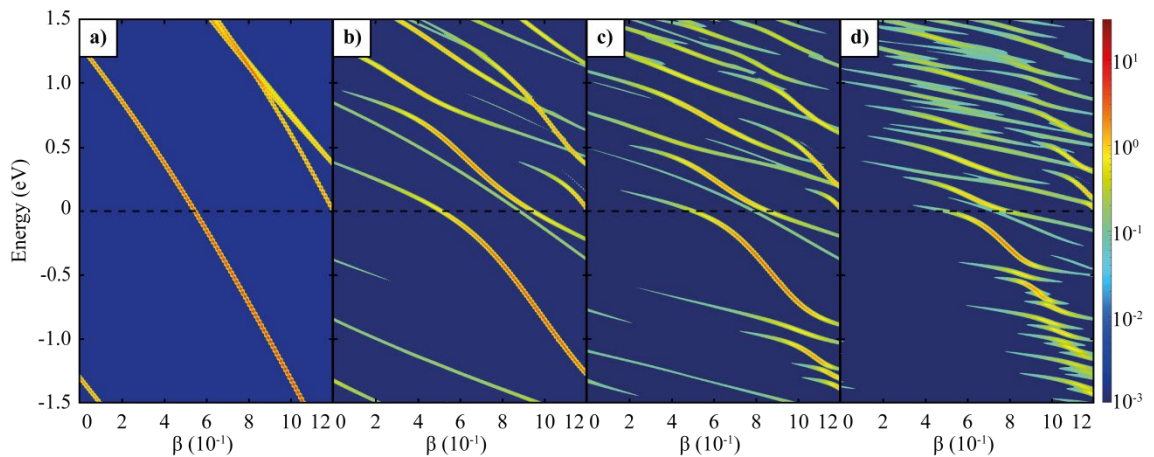


Figure 3.3. LDOS of the impurity center for a) 42, b) 546, c) 1626, and d) 5514 atoms in TB.

As seen in Fig. 3.3. that at an increasing size of the GQD, the R1 resonance state becomes more observable at the supercritical regime. However, in the smaller GQDs, the maximum of the LDOS followed collapse of TLBS which used in the work of Polat et al. Additionally, TLBS contributes first to R1 state at the supercritical regime.

Introducing MFH results to the smaller GQDs negligibly changed the LDOS. A small shift in the value of the impurity charge is still present in the LDOS of the MFH results. Although it is dependent on the location of the eigenvalues, magnitude of the LDOS of the energy states resembled similarity to the TB results as in Fig. 3.3.

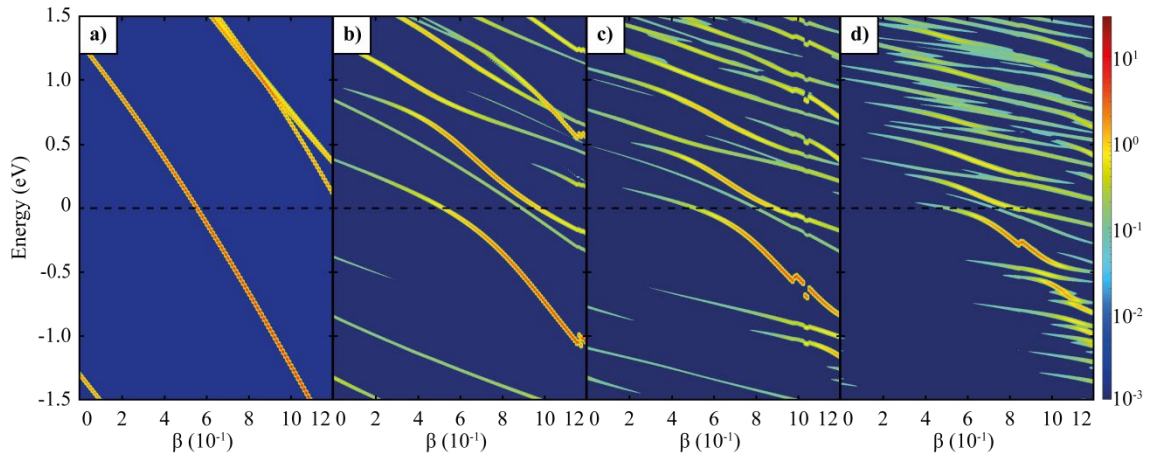


Figure 3.4. LDOS of the impurity center for a) 42, b) 546, c) 1626, and d) 5514 atoms in MFH.

### 3.2 Effect of the External Magnetic field to Atomic Collapse

In this section, we introduce the external magnetic field to the charged impurity problem. To compare results between varying-sized GQDs, we used magnetic length ( $l_B$ ) to relate to the radius of the GQDs ( $R_{GQD}$ ). It is known that energy states become Landau levels (LLs) in a uniform magnetic field. Moldovan et al. showed that atomic collapse in a uniform magnetic field resulted in resonance states formed from discrete LLs rather than a continuum form as in Fig. 1.5. Referring to the work of Polat et al. and Moldovan et al., we stressed the TLBS and formation of R1 state under magnetic field while adjusting the GQD size. Without the impurity charge, it is expected the LLs

that are resided close to 0 eV forms when the  $l_B < R_{\text{GQD}}$ . Using the magnetic length formula, we noted Table 1 below that the required magnetic field for the  $l_B = R_{\text{GQD}}$ .

Number of the Atoms	Flake Radius (nm)	Expected Magnetic Field for Landau Level Formation (T)
42	0.568	2095.32
114	0.994	684.19
222	1.42	335.25
546	2.272	130.96
1626	3.976	42.76
3282	5.677	20.98
5514	7.384	12.4
6162	7.81	11.08
7566	8.66	9.01
8322	9.09	8.18
10806	10.366	6.29

Table 1. The number of atoms, radius, and Expected Landau Level Formation according to the magnetic length formula equivalence for the considered structures.

We tested several sizes of the  $l_B$  where the  $l_B$  smaller and larger than the size of the radius. Introducing the magnetic field to the charged impurity, altered the crossing point of the Fermi level to each GQD differently. As we discussed earlier, increasing the size of the GQD, converges the energy levels to the Fermi level including TLBS. As seen in Fig. 3.5. that TLBS has lower energy than Fermi level in increasing GQD size and magnetic field. In other words, the  $\beta_c$  required for TLBS to become lower than the Fermi level decreased when the radius of the GQD and the strength of the magnetic field increased. Moreover, GQD with increasing radius in a uniform magnetic field showed similarity to the LL formation at  $E = 0$  eV for bulk Graphene.

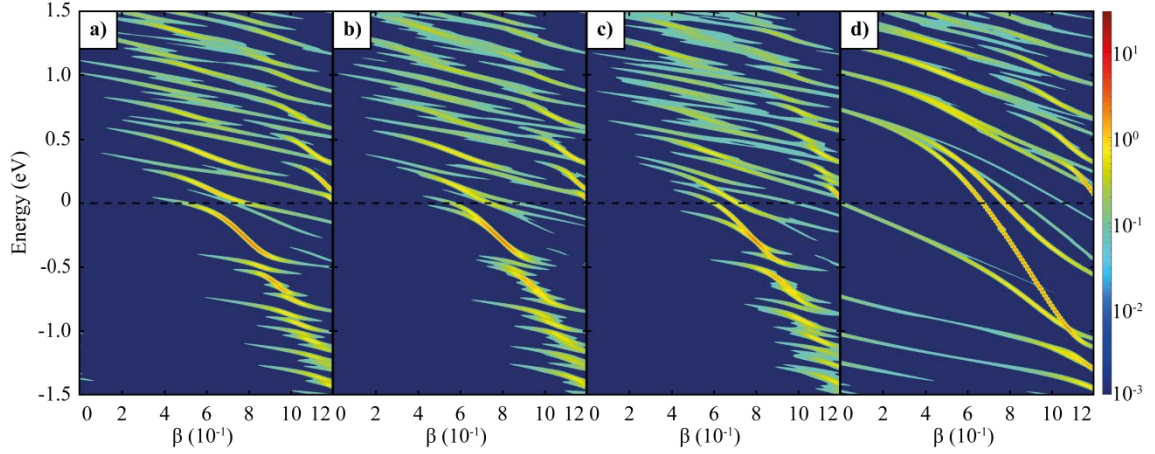


Figure 3.5. LDOS of the impurity center of the 5514 atom QD in a external magnetic field of a) 0 T, b) 10 T, c) 25T, and d) 250 T in TB.

In Fig. 3.5., that we employed a uniform magnetic field for QDs with finite radius. In the study of Moldovan et al., they used bulk Graphene, and they applied a magnetic field much smaller than what we have used in the calculations. We related the reason for discrete LLs to become more prominent to magnetic length via magnetic field (Eq. 2.50). It can be assumed theoretically that the radius of bulk Graphene is infinite. No magnetic field case leads to no magnetic length, and according to Eq. 2.50. that magnetic length can be assumed as infinite. However, introducing a magnetic field immediately resulted in a finite magnetic length, that is smaller than the radius of Graphene where the LLs are noticeable. QDs have a finite radius, where we compare the magnetic field via the  $l_B$  to identify the evolution of the notability of LLs in charged impurity. In Figs. 3.5. and 3.6, we used a QD with the radius of 7.38 nm and  $\mathbf{B}$  of 0, 10, 25, and 250 T where  $l_B$  are  $\infty$ , 8.22, 5.20, and 3.00 nm, respectively. For  $\mathbf{B} = 0$  and 10 T cases,  $l_B > R_{\text{QD}}$ , however, for  $\mathbf{B} = 25$  T case where  $l_B < R_{\text{QD}}$ , the form of the R1 state is negligibly changed in both TB and MFH methods in Figs. 3.5. and 3.6. For both  $\mathbf{B} = 10$  and 25 T cases, separation of LLs has similarity to the  $B = 2$  T case of Fig. 1.5.

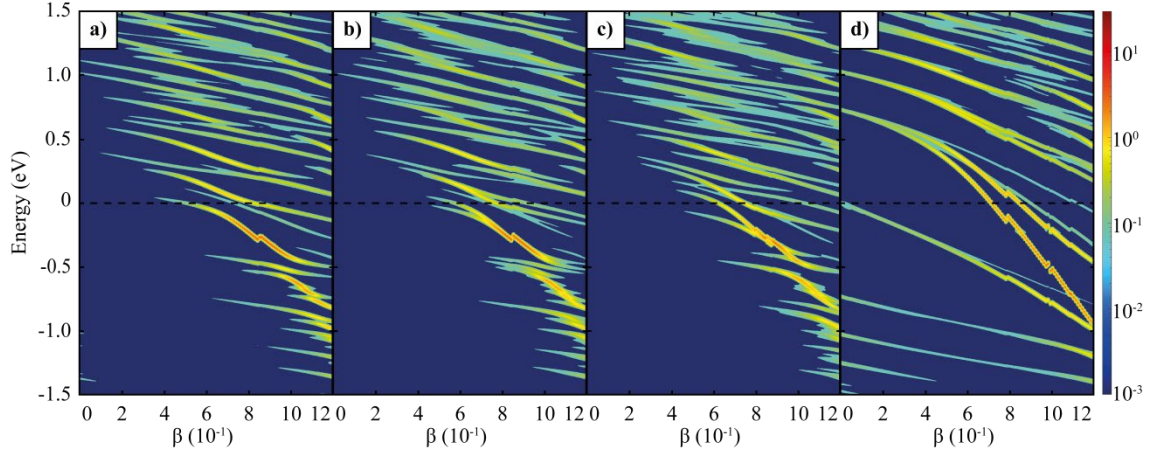


Figure 3.6. LDOS of the impurity center of the 5514 atom GQD in an external magnetic field of a) 0 T, b) 10 T, c) 25 T, and d) 250 T in MFH.

Employing MFH, we identified similar results as we did without a magnetic field, which is the collapsing of the lower energy required to the slightly greater charge at the supercritical regime where  $\beta > 1$ . Meanwhile, the magnetic field resulted in TLBS decrease below the Fermi level at the subcritical regime. Additionally, at higher magnetic fields inter-level spacing between LLs is noticeable (Figs. 3.5. (d) and 3.6. (d)). Moreover, the form of the R1 state significantly changed to the other situations. In a way,  $\mathbf{B} = 250$  T for this GQD has a similarity to the  $\mathbf{B} = 12$  T case of the bulk Graphene. After the LDOS of the impurity center for varying magnetic fields and GQDs was calculated, we compared our results for GQDs with varying sizes. As you can see in Fig. 3.7., we plotted the location of the R1 state formations which originated from TLBS at the subcritical regime and following the location of the maximum of the LDOS at the spectrum of eigenvalue energy and impurity charge.

As seen in Fig. 1.4. that Polat et al. indicated the  $\beta_c$  of the GQDs with varying sizes by a blue dashed line. We employed the same reasoning for the no magnetic field case by red dashed line. When a magnetic field is introduced, the  $\beta_c$  requires TLBS to become lower than the Fermi levels changed. Additionally, the shift on the  $\beta_c$  depends on the size of the GQD. We found that the multiple  $\beta_c$  of the GQDs with varying sizes in a uniform magnetic field are different from each other. On the other hand, we found another relation with consideration of the  $l_B$ .

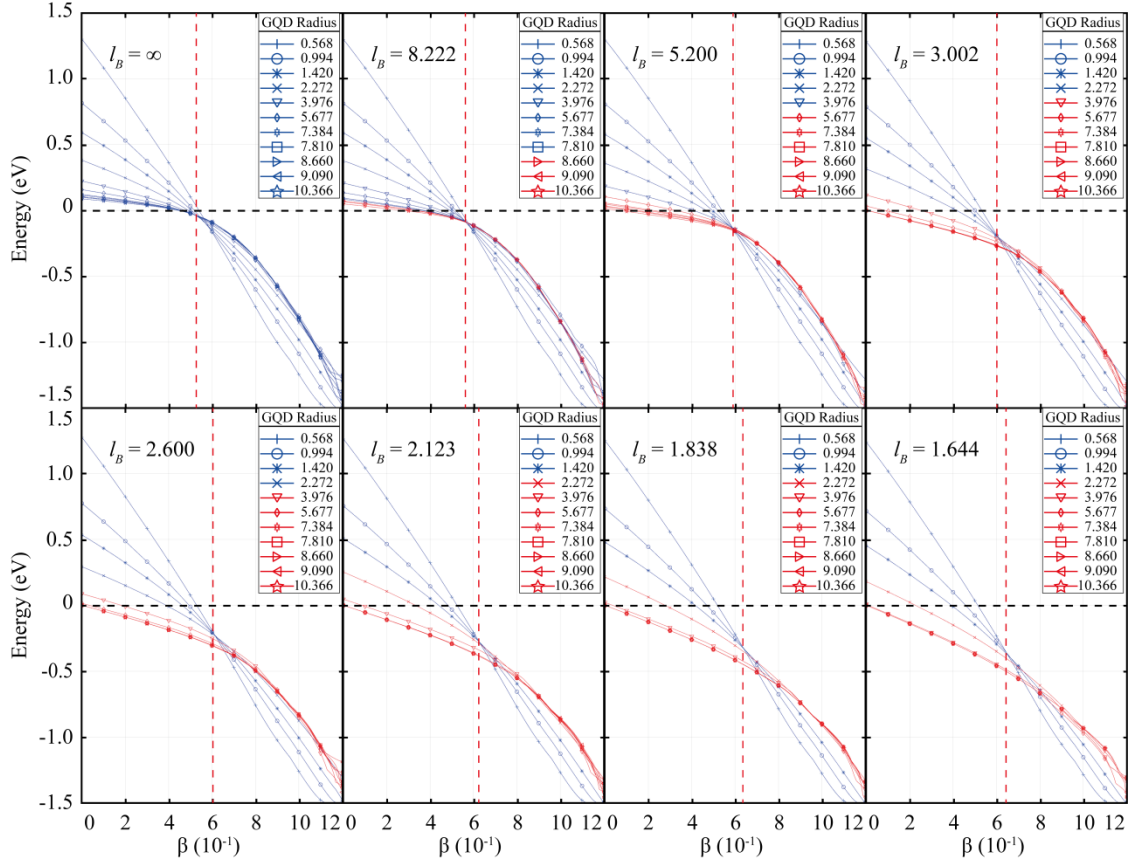


Figure 3.7. The plot of the R1 resonance states for varying GQD for decreasing  $l_B$  (increasing  $\mathbf{B}$ ) in TB. Red lines referring to  $l_B < R_{\text{GQD}}$  and Blue lines referring to  $l_B > R_{\text{GQD}}$ . Vertical dashed red line correspond to the crossing of the TLBS.  $l_B$  and  $R_{\text{GQD}}$  in units of nm.

In the Figs. 3.7. and 3.8., we plotted the evolution of the R1 state with blue lines when  $l_B > R_{\text{GQD}}$  and red lines when  $l_B < R_{\text{GQD}}$ . At  $\mathbf{B} = 0$  T, TLBS of all GQDs meets at a certain point where we refer it as the crossing point (CP). In  $\mathbf{B} = 0$  T case, the CP has  $E = 0$  and  $\beta = 0.5$ . Implementing magnetic field, where  $l_B > R_{\text{GQD}}$  still meets at a certain point while the energy and the charge of the CP are different from the  $\mathbf{B} = 0$  T case.

On the other hand, TLBS started to diverge from the CP when  $l_B < R_{\text{GQD}}$ . In Figs. 3.7. and 3.8., we can see TLBS significantly diverged from the CP when  $l_B$  is highly smaller than the  $R_{\text{GQD}}$ . In extreme magnetic fields for a GQD in which the  $l_B$  is much smaller than the  $R_{\text{GQD}}$ , resulted to not only TLBS significantly diverged from the CP but also we refer to our previous findings. In this case, we can see the formation of the R1 formed from inter-level spaced LLs. Additionally, a small impurity charge is enough for TLBS to become lower than the Fermi level.

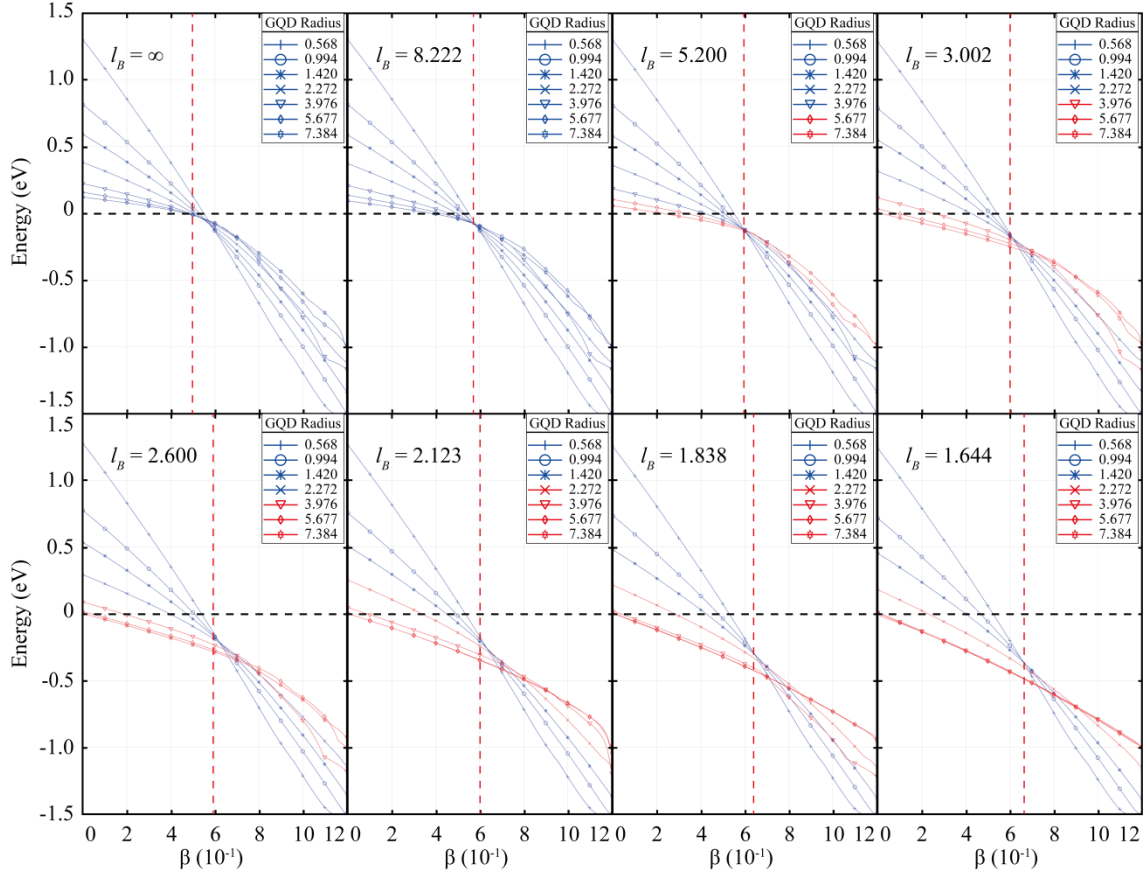


Figure 3.8. The plot of the R1 resonance states for varying GQD for decreasing  $l_B$  (increasing  $\mathbf{B}$ ) in MFH. Red lines referring to  $l_B < R_{\text{GQD}}$  and Blue lines referring to  $l_B > R_{\text{GQD}}$ . Vertical dashed red line correspond to the crossing of the TLBS.  $l_B$  and  $R_{\text{GQD}}$  in units of nm.

As you can see in Fig. 3.8., we Implemented MFH calculations to the GQDs. The MFH confirmed the TB findings. Although the slight shift in critical charge is still present, physical results remained the same.

Furthermore, we investigated the probability density of the evolution of TLBS to the R1 state in varying critical regimes. We presented our results for  $l_B > R_{\text{GQD}}$  in 3.9., for  $l_B < R_{\text{GQD}}$  in 3.10 in TB. Lastly, we provided MFH results in Fig. 3.11. We also noted that a different color scale is preferred than what we have used in the LDOS plots. Due to the high difference in color scale among the results, each figure is set to the maximum probability density of individual cases.

In Fig. 3.9. (a), TLBS is plotted without magnetic field and atomic collapse effects. In this case, the difference of probability density distribution around all atoms is more minimal in comparison to the other cases. The probability density of atomic

collapse effect without magnetic field is plotted in Fig. 3.9. (b,c, and d). In a subcritical regime ( $\beta = 0.4$ ), the probability density of charged impurity is localized around the impurity center (Fig. 3.9. (b)). However, the probability density of TLBS is observable in the remaining atomic sites, also. At critical charge ( $\beta = 0.5$ , in Fig. 3.9. (c)), a more localized probability density at the impurity center is noticeable than in the subcritical case. This localization has more magnitude in terms of probability density, and have more probability density difference to the remaining atomic sites. In Fig. 3.9. (d), the probability density of the R1 state at  $\beta = 1$  without a magnetic field is plotted. A significant localization at the impurity center is present. The magnitude of the probability density is greatly increased, and the difference of the probability density to the remaining atomic sites is increased.

The  $l_B > R_{GQD}$  for  $\mathbf{B} = 10$  T case is plotted in Figs. 3.9. (e, f, g, and h). In Fig. 3.9. (e), TLBS is plotted with a 10 T magnetic field and without an impurity charge. In this case, the difference of probability density distribution around all atoms is more minimal in comparison to the cases with increasing impurity charge. Although the magnitude of the probability density is slightly different from the case without a magnetic field, magnetic field effects are minimal to TLBS. In a subcritical regime ( $\beta = 0.4$ ), the probability density of charged impurity is localized around the impurity center (Fig. 3.9. (f)). In this situation, we noted from Figs. 3.7. and 3.8. that magnetic field lowered the critical requirement for TLBS becomes lower than the Fermi Level. Thus, the magnetic field has increased the localization of the probability density at the impurity center. However, the probability density of TLBS is observable in the remaining atomic sites.

At  $\beta = 0.5$  with  $\mathbf{B} = 10$  T as in Fig. 3.9. (g), a more localized probability density at the impurity center is noticeable than in  $\beta = 0.4$ . This localization has more magnitude in terms of probability density, and have more probability density difference to the remaining atomic sites. In Fig. 3.9. (h), the probability density of the R1 state at  $\beta = 1$  with a  $\mathbf{B} = 10$  T is plotted. A significant localization at the impurity center is present. The magnitude of the probability density is greatly increased, and the difference of the probability density to the remaining atomic sites is increased.

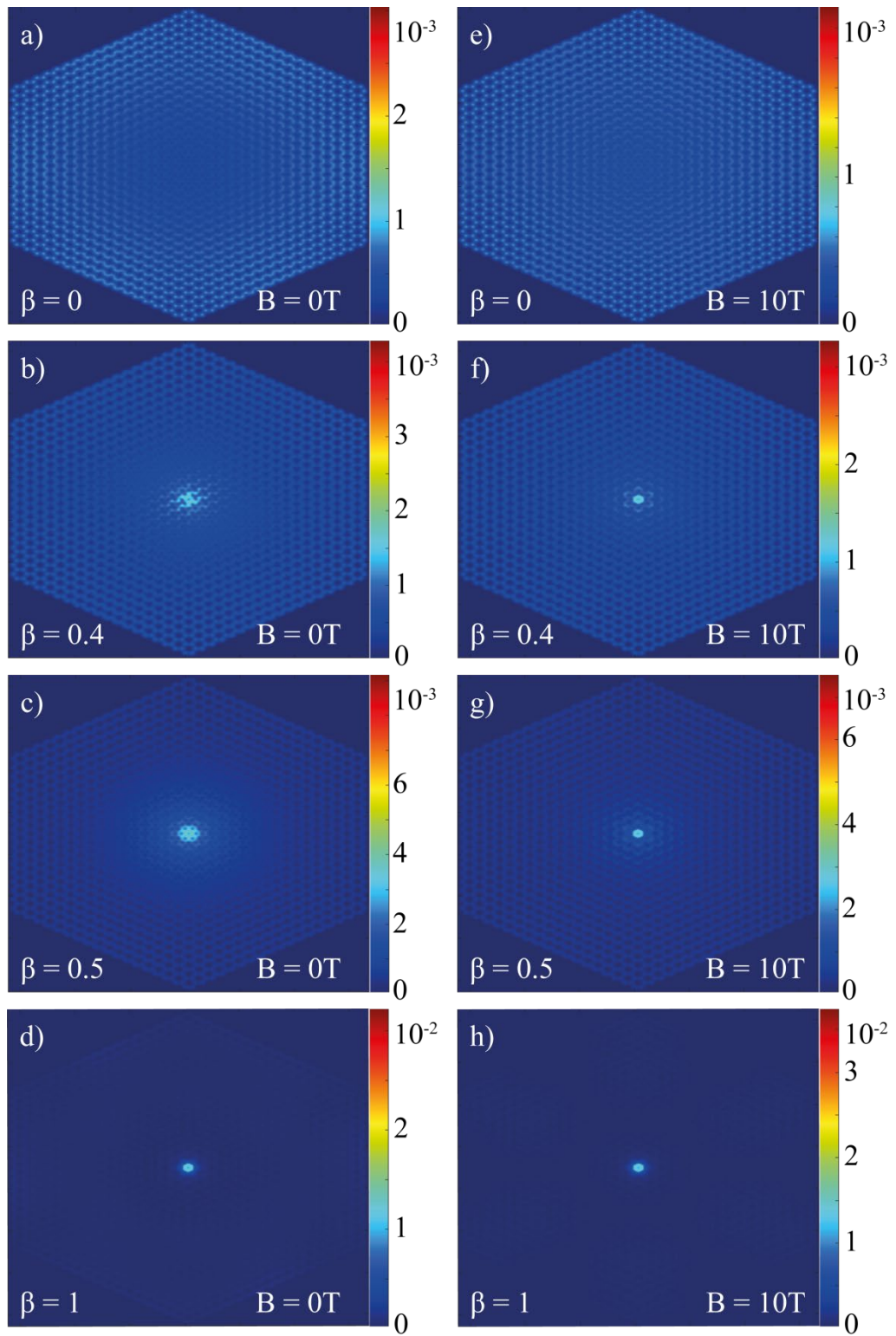


Figure 3.9. The probability density of the evolution of the R1 States for 5514 atom GQD where  $l_B > R_{\text{GQD}}$ .

The  $l_B < R_{GQD}$  for  $\mathbf{B} = 25$  T case is plotted in Figs. 3.10. (a, b, and h) In Fig. 3.9. (a), TLBS is plotted with a 25 T magnetic field and without an impurity charge. In this case, the difference of probability density distribution around all atoms is more minimal in comparison to the cases with increasing impurity charge. Although the magnitude of the probability density is slightly different from the cases with  $\mathbf{B} = 0$  and 10 T, magnetic field effects are minimal to TLBS. At  $\beta = 0.5$  as in Fig. 3.10. (b), a localized probability density at the impurity center is noticeable. In Fig. 3.10. (c), the probability density of the R1 state at  $\beta = 1$  with a  $\mathbf{B} = 25$  T is plotted. A significant localization at the impurity center is present. The magnitude of the probability density is greatly increased, and the difference of the probability density to the remaining atomic sites is increased. Although in  $\mathbf{B} = 25$  T case  $l_B < R_{GQD}$ , magnetic fields effects negligibly changed in comparison to  $\mathbf{B} = 10$  T.

The  $l_B < R_{GQD}$  for  $\mathbf{B} = 250$  T case is plotted in Figs. 3.10. (d, e, and f) In Fig. 3.9. (d), TLBS is plotted with a 25 T magnetic field and without an impurity charge. In this case, the difference of probability density distribution around all atoms is more minimal in comparison to the cases with increasing impurity charge. Although the magnitude of the probability density is slightly different from the case with  $\mathbf{B} = 0$  and 10 T, magnetic field effects are minimal to TLBS. At  $\beta = 0.5$  as in Fig. 3.10. (e), a localized probability density at the impurity center is noticeable. However, the probability density at the remaining atomic sites has differed from other magnetic field situations. Thus, the probability density is noticeable close to the impurity center, and it is noticeable at the edge of the GQD. In Fig. 3.10. (f), the probability density of the R1 state at  $\beta = 1$  with a  $\mathbf{B} = 250$  T is plotted. A significant localization at the impurity center is present. The magnitude of the probability density is greatly increased, and the difference of the probability density to the remaining atomic sites is increased as in  $\mathbf{B} = 0, 10,$  and 25 T. Although the R1 state formation is expected to be formed in inter-level spaced LLs, the robustness of the atomic collapse is present in the probability density.

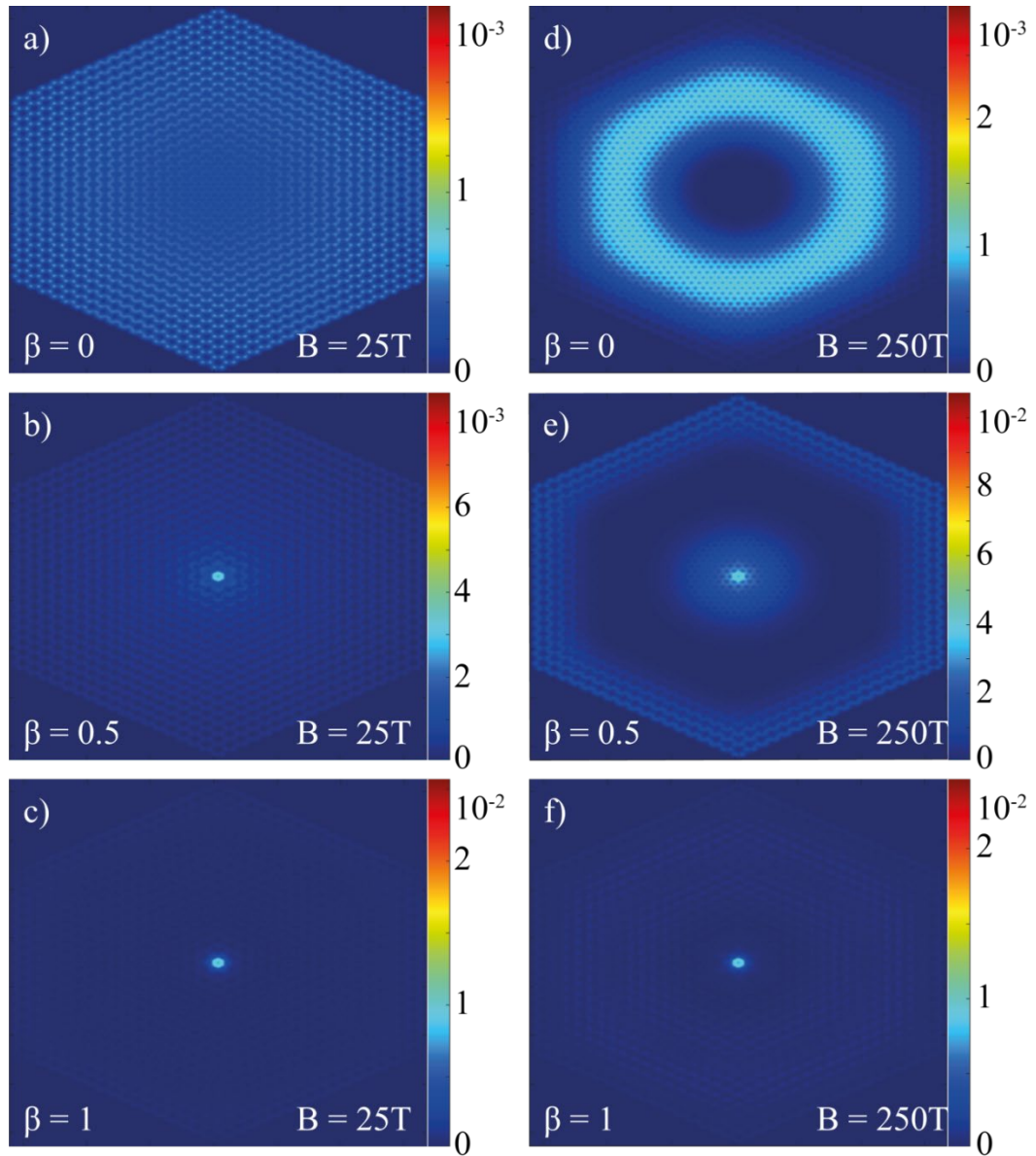


Figure 3.10. The probability density of the evolution of the R1 States for 5514 atom GQD where  $l_B < R_{GQD}$ .

We employed MFH in the probability density calculations, as seen in Fig. 3.11. MFH resulted in significantly closer to TB results in terms of the evolution of the probability density. In both methods, the increase of the impurity charge resulted in localized probability density at the impurity center. Also, the difference of probability density between the impurity center and remaining sites increased with incrementing the impurity charge. One notable difference between both MFH and TB methods is a slight difference at the maximum probability density.

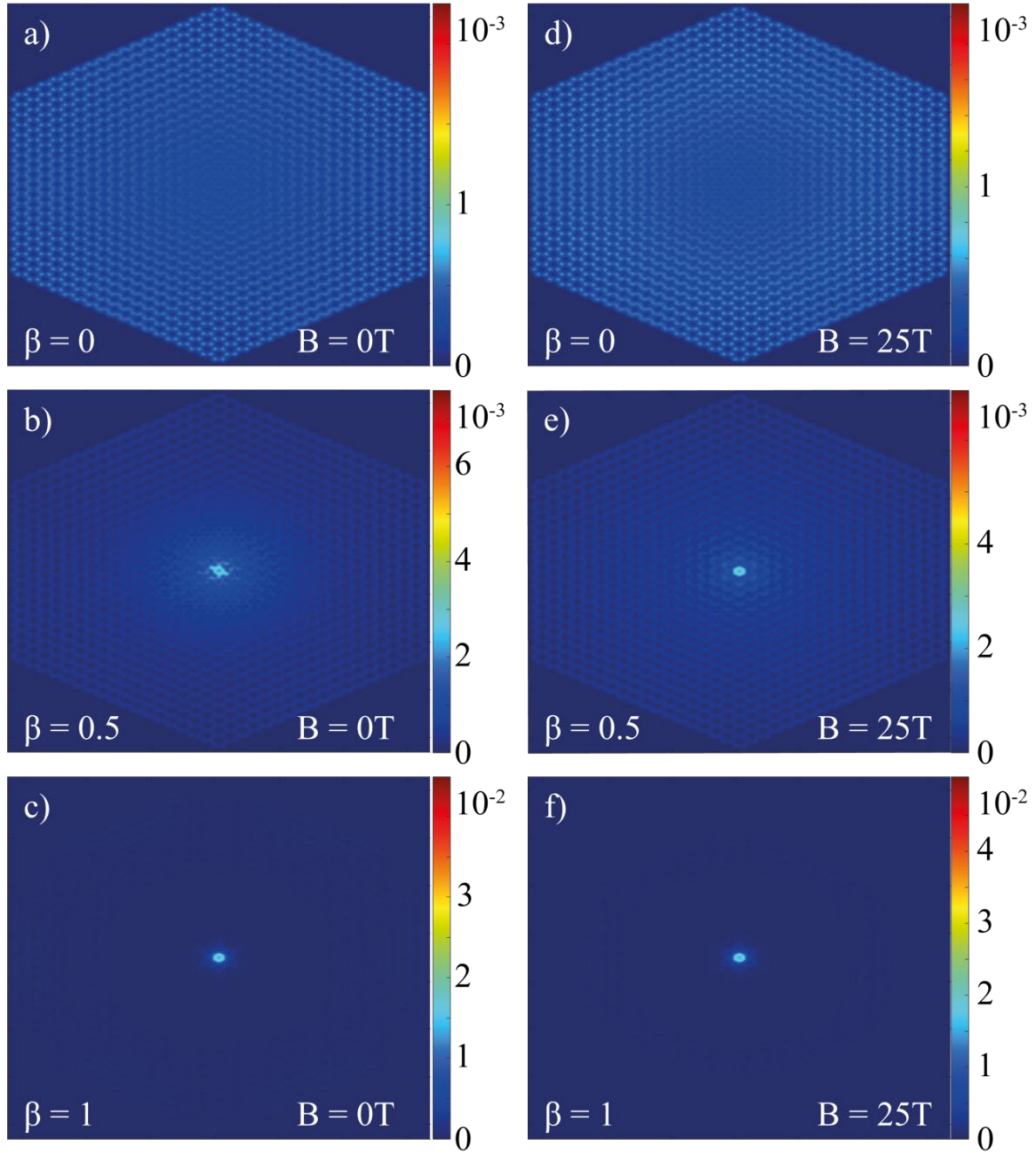


Figure 3.11. The probability density of the evolution of the R1 States for 5514 atom GQD for  $l_B$  is larger (a, b, c) and smaller (d, e, f) than the  $R_{GQD}$  with MFH.

### 3.3. Atomic Collapse of Hofstadter's Butterfly

In this section, we investigated the influence of the varying magnetic fields and a static impurity charge on the eigenenergies of the GQDs. The energy and magnetic field spectrum for the Pierels phase (Eq. 2.13) considered where the phase is in between 0 and 1 are investigated. We calculated the spectrum for GQDs in varying sizes where the

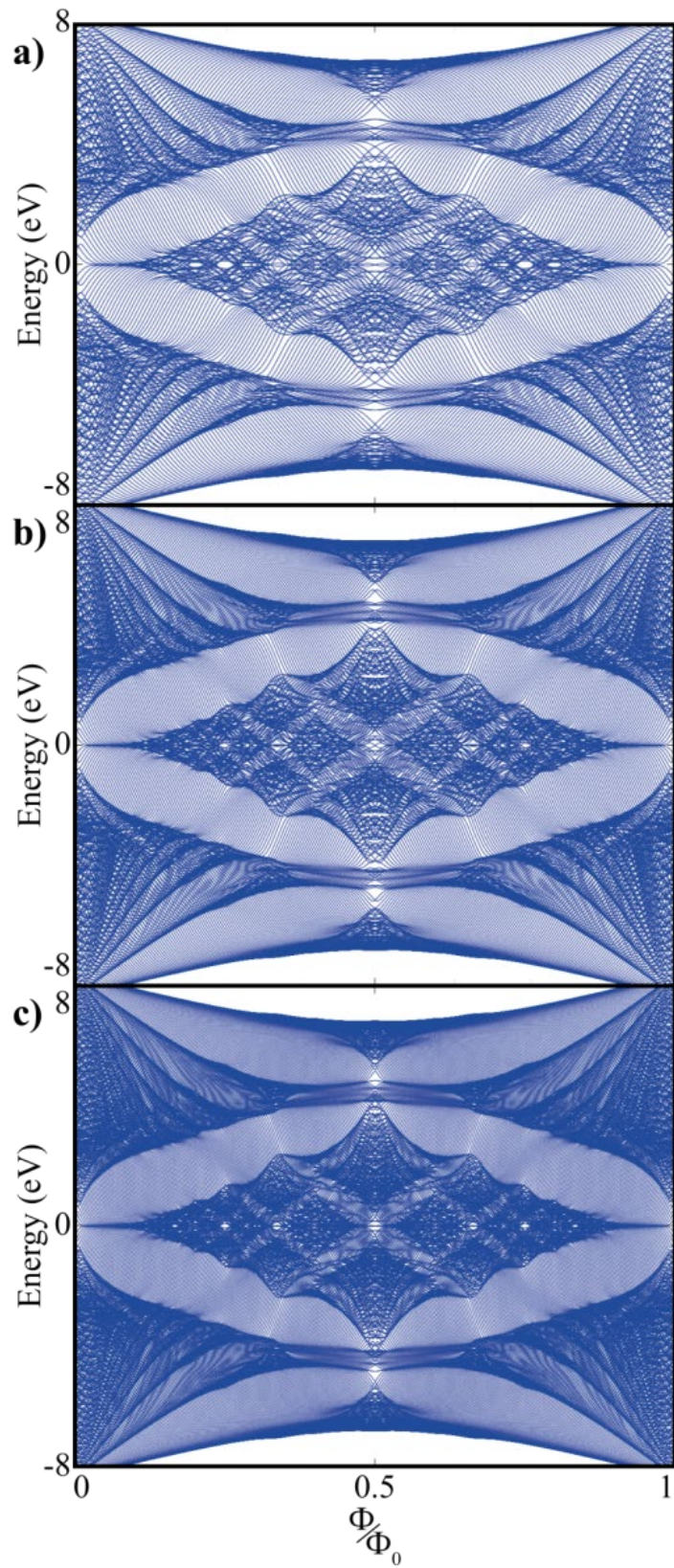


Figure 3.12. Energy vs magnetic flux spectrum of Hofstadter's butterflies for the a) 366, b) 546, c) 762 atom GQDs.

spectrum corresponds to Hofstadter's butterfly (HB). We implemented a static charge impurity to the HBs and studied the LDOS of the impurity center on top of the spectrum of the HBs as you can see in Figs 3.13. and 3.14.

We plotted the HBs for varying GQDs as in Fig. 3.12. Increasing the number of atoms in GQDs negligibly altered the characteristics of the HBs. We calculated the HBs without an atomic collapse effect in Fig. 3.12. The spectrum is filled with more energy levels at bigger GQDs. As you can see the involvement of the energy levels into the inner butterflies increased by the size of the GQDs. For a GQD with  $R_{GQD} = 7.384$  nm and the number of atoms is 5514, the finite size effect resulted in an unclear spectrum of the HBs. Implementation of the LDOS calculations to the HBs (as we used in Figs. 3.3., 3.4., 3.5., and 3.6.) resulted in figures that are free from finite-size effect of the energy levels (as you can see in Figs. 3.13. and 3.14.). Apart from the number of atoms of the GQD, the LDOS figure (Fig. 3.13.) negligibly filled with the energy levels as in Fig. 3.12.

In earlier sections, we investigated the effect of charged impurity on the energy levels and the LDOS of the impurity center. Applied static impurity charge to the HBs, has notable differences at the whole spectrum. We considered the subcritical regime at Figs. 3.13. (a and b) and 3.14. (a and b), and the supercritical regime at Figs. 3.13. (c and d) and 3.14. (c and d). The result for the LDOS of the impurity center of HB without impurity charge is seen in Fig. 3.13. (a). It is seen that the LDOS is distributed symmetrically over the HB spectrum. We can also note that the LDOS of the impurity center of a GQD is almost similar to the HB of the bulk Graphene (Rhim et al. (2012)). At the subcritical regime ( $\beta = 0.4$  in Fig. 3.13. (b)), it is seen that the energy levels and the LDOS affected by the atomic collapse. Additionally, the symmetrical distribution of the LDOS showed a difference to the  $\beta = 0$  case.

HB in the supercritical regime (at  $\beta = 0.8$ ), It is notable that the atomic collapse effect is increased further (Fig. 3.13. (c)). Additionally, we noted a new distributional characteristic of the LDOS of the impurity center. Although the eigenenergies of the HBs are decreased with the presence of the charged impurity, LDOS appeared to be increased at the lower half of the HBs. On the other hand, LDOS at the upper half of the HBs is decreased. In  $\beta = 1.2$  (Fig. 3.13. (d)), the LDOS significantly became more prominent at the lower half of the HB.

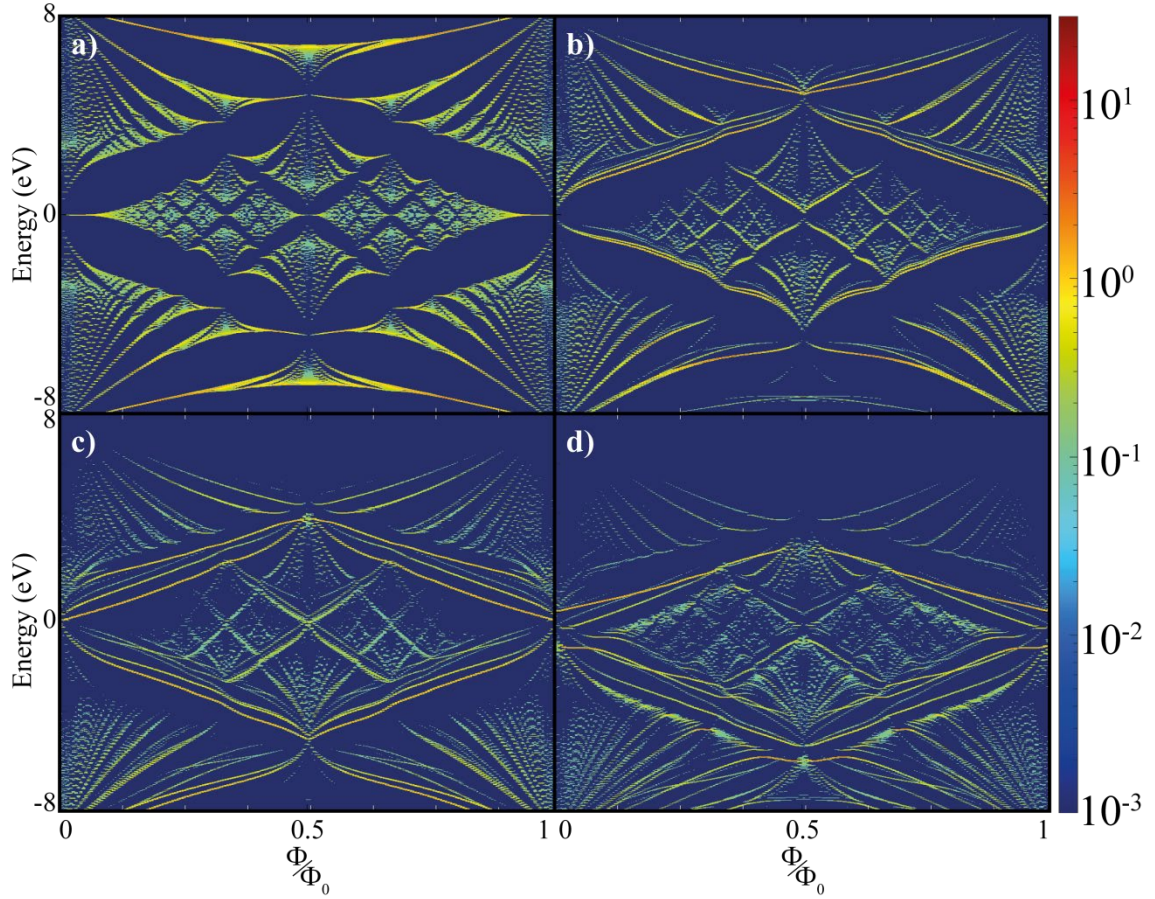


Figure 3.13. LDOS of the impurity center of Hofstadter's butterflies for the a)  $\beta = 0$ , b)  $\beta = 0.4$ , c)  $\beta = 0.8$ , and d)  $\beta = 1.2$  of 5514 atom GQD in TB.

Furthermore, we are concerned about the atomic collapse effect on HBs with MFH, as seen Fig. 3.14. Calculations in the MFH method resulted in similar characteristics as found in the TB method. Symmetrical distribution of the LDOS of the impurity center in HB is found at  $\beta = 0$ . Including an impurity, charge affected the energy levels and LDOS of the impurity center. Increasing the impurity charge resulted in increased LDOS at the lower half of the HB while decreased LDOS at the upper half of the HB.

As seen in Fig. 3.14. (a), the on-site potential due to the spin-spin interaction resulted in a small energy gap at the vicinity of the Fermi level for  $\beta = 0$ . However, it is seen from Figs. 3.14. (b, c, and d), increasing the impurity charge alleviated the gap.

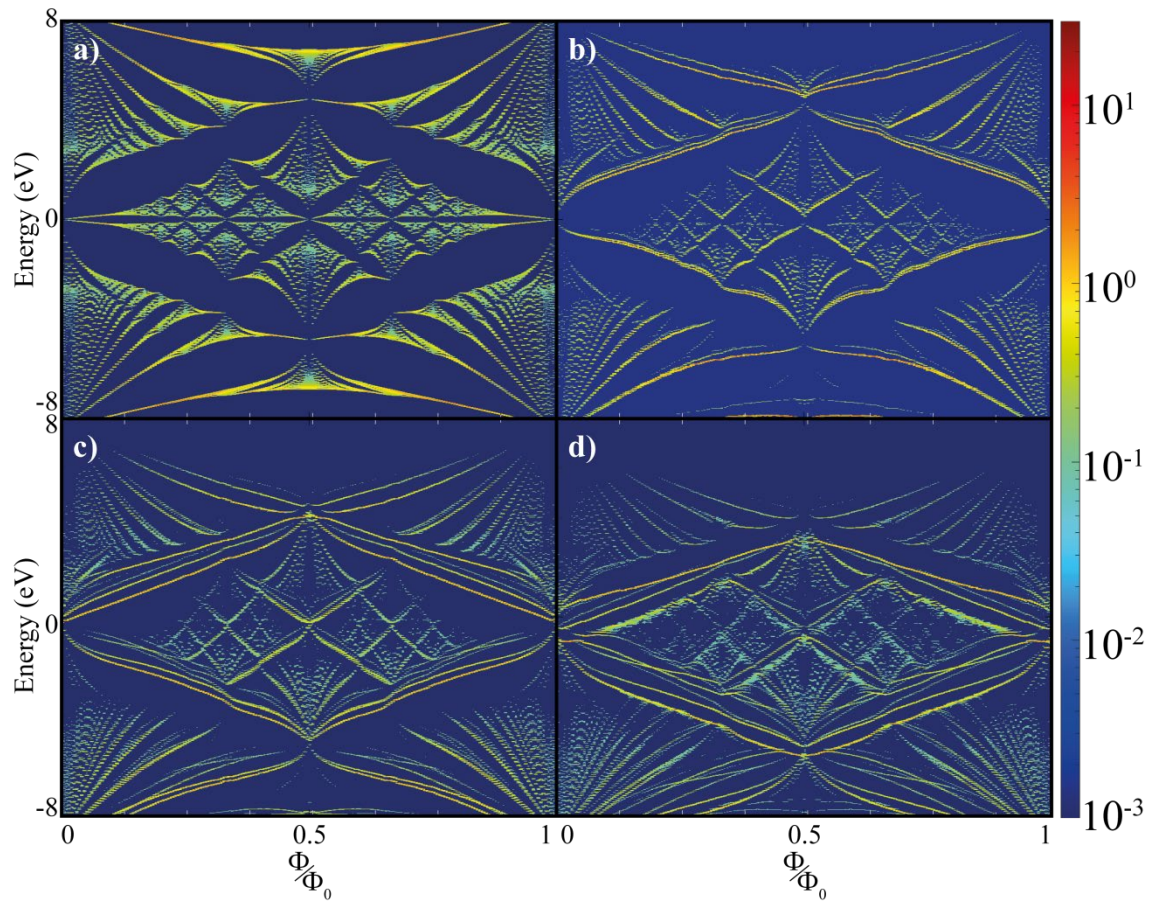


Figure 3.14. LDOS of the impurity center of Hofstadter's butterflies for the a)  $\beta = 0$ , b)  $\beta = 0.4$ , c)  $\beta = 0.8$ , and d)  $\beta = 1.2$  of 5514 atom GQD in MFH.

## CHAPTER 4

### CONCLUSION

In this thesis, we employed TB and MFH methods to investigate the atomic collapse of GQDs in a magnetic field. We started by confirming earlier results. Applying a perpendicular magnetic field to GQD decreased the  $\beta_c$  of each structure, and we found that the decrease is dependent on the dot size. It was shown that TLBS of GQDs had a similar critical charge that crosses the Fermi level. Although, the critical charge changes in a magnetic field, we found that TLBS converged to each other at a certain eigenenergy and impurity charge. We found that TLBS diverged the point when the  $l_B < R_{GQD}$ . It is shown that the R1 state formed in a series of LLs in the magnetic field. We show that LL formation and the increase of the inter-level space of the LLs improved when the  $l_B < R_{GQD}$ . Additionally, we showed the robustness of the atomic collapse effect of the impurity center at probability density calculations. We found that the magnetic field negligibly affected the evolution of the probability density of the R1 state. Lastly, we studied that atomic collapse has an impact on the energy spectrum and LDOS of the Hofstadter's butterflies. The change on the spectrum and the LDOS improved further when the impurity charge increases.

## REFERENCES

- Akgenc, B. Intriguing of two-dimensional Janus surface-functionalized MXenes: An ab initio calculation. *Computational Materials Science* **2020**, 171, 109231.
- Altıntaş, A.; Güçlü, A. D. Defect induced Anderson localization and magnetization in Graphene quantum dots. *Solid State Communications* **2018**, 281, 44-48.
- Baskurt, M.; Eren, I.; Yagmurcukardes, M.; Sahin, H. Vanadium dopant-and strain-dependent magnetic properties of single-layer VI3. *Applied Surface Science* **2020**, 508, 144937.
- Chao, D.; Zhu, C.; Xia, X.; Liu, J.; Zhang, X.; Wang, J.; Liang, P.; Lin, J.; Zhang, H.; Shen, Z. X.; Fan, H. J. Graphene quantum dots coated VO2 arrays for highly durable electrodes for Li and Na ion batteries. *Nano letters* **2015**, 15(1), 565-573.
- Chen, B.; Liu, E.; Cao, T.; He, F.; Shi, C.; He, C.; Ma, L.; Li, Q.; Li, J.; Zhao, N. Controllable Graphene incorporation and defect engineering in MoS2-TiO2 based composites: towards high-performance lithium-ion batteries anode materials. *Nano Energy* **2017**, 33, 247-256.
- Choi, D. S.; Kim, C.; Lim, J.; Cho, S. H.; Lee, G. Y.; Lee, H. J.; Choi, J. W.; Kim, H.; Kim, I.; Kim, S. O. Ultrastable Graphene-Encapsulated 3 nm Nanoparticles by In Situ Chemical Vapor Deposition. *Advanced Materials* **2018**, 30(51), 1805023.
- Chung, D. D. L. Review graphite. *Journal of materials science* **2002**, 37(8), 1475-1489.
- Cowan, T.; Backe, H.; Begemann, M.; Bethge, K.; Bokemeyer, H.; Folger, H.; Greenberg, J. S.; Grein, H.; Gruppe, A.; Kido, Y.; Klüver, M.; Schwalm, D.; Schweppe, J.; Stiebing, K. E.; Trautmann, N.; Vincent, P. Anomalous positron peaks from supercritical collision systems. *Physical Review Letters* **1985**, 54(16), 1761.

Çakmak, K. E.; Altıntaş, A.; Güçlü, A. D. Effects of random atomic disorder on the magnetic stability of Graphene nanoribbons with zigzag edges. *Physical Review B* **2018**, 98(11), 115428.

De Volder, M. F.; Tawfick, S. H.; Baughman, R. H.; Hart, A. J. Carbon nanotubes: present and future commercial applications. *Science* **2013**, 339(6119), 535-539.

Dong, Y.; Yang, S.; Zhang, Z.; Lee, J. M.; Zapien, J. A. Enhanced electrochemical performance of lithium ion batteries using Sb<sub>2</sub>S<sub>3</sub> nanorods wrapped in Graphene nanosheets as anode materials. *Nanoscale* **2018**, 10(7), 3159-3165.

Eren, I.; İyikanat, F.; Sahin, H. Defect tolerant and dimension dependent ferromagnetism in MnSe<sub>2</sub>. *Physical Chemistry Chemical Physics* **2019**, 21(30), 16718-16725.

Ge, J.; Lan, M.; Zhou, B.; Liu, W.; Guo, L.; Wang, H.; Jia, Q.; Niu, G.; Huang, X.; Zhou, H.; Meng, X.; Wang, P.; Lee, C.-S.; Zhang, W.; Han, X. A Graphene quantum dot photodynamic therapy agent with high singlet oxygen generation. *Nature communications* **2014**, 5(1), 1-8.

Griffiths, D. J.; Schroeter, D. F. *Introduction to quantum mechanics*. Cambridge University Press, 2018.

Güçlü, A. D.; Hawrylak, P. Optical control of magnetization and spin blockade in Graphene quantum dots. *Physical Review B* **2013**, 87(3), 035425.

Güçlü, A. D.; Potasz, P.; Korkusinski, M.; Hawrylak, P. *Graphene quantum dots*, Springer, 2014.

Hubbard, J. Electron correlations in narrow energy bands. A. *Mathematical and Physical Sciences* **1963**, 276(1365), 238-257.

Hofstadter, D. R. Energy levels and wave functions of Bloch electrons in rational and irrational magnetic fields. *Physical review B* **1976**, 14(6), 2239.

Kul, E. B.; Polat, M.; Güçlü, A. D. Electronic and magnetic properties of Graphene quantum dots with two charged vacancies. *Solid State Communications* **2020**, 322, 114096.

Li, Y.; Yan, K.; Lee, H. W.; Lu, Z.; Liu, N.; Cui, Y. Growth of conformal Graphene cages on micrometre-sized silicon particles as stable battery anodes. *Nature Energy* **2016**, 1(2), 1-9.

Moldovan, D.; Masir, M. R.; Peeters, F. M. Magnetic field dependence of the atomic collapse state in Graphene. *2D Materials* **2017**, 5(1), 015017.

Moldovan, D.; Peeters, F.; Masir, M. R. Electronic properties of strained Graphene and supercritical charge centers. Ph.D. Thesis, University of Antwerp, Antwerp, Belgium, 2016.

Neto, A. C.; Guinea, F.; Peres, N. M.; Novoselov, K. S.; Geim, A. K. The electronic properties of Graphene. *Reviews of modern physics* **2009**, 81(1), 109.

Novoselov, K. S.; Geim, A. K.; Morozov, S. V.; Jiang, D.; Zhang, Y.; Dubonos, S. V.; Grigorieva, I. V.; and Firsov, A. A. *Electric field effect in atomically thin carbon films. Science* **2004**, 306(5696), 666-669.

Novoselov, K. S.; Jiang, Z.; Zhang, Y.; Morozov, S. V.; Stormer, H. L.; Zeitler, U.; J. Maan, C.; Boebinger, G. S.; Kim, P.; Geim, A. K. Room-temperature quantum Hall effect in graphene. *Science* **2007**, 315(5817), 1379-1379.

Peierls, R. Zur theorie des diamagnetismus von leitungselektronen. *Zeitschrift für Physik*, 80(11-12) **1933**, 763-791.

Polat, M.; Sevinçli, H.; Güçlü, A. D. Collapse of the vacuum in hexagonal Graphene quantum dots: A comparative study between tight-binding and mean-field Hubbard models. *Physical Review B* **2020**, 101(20), 205429.

Reinhardt, J.; Greiner, W. Quantum electrodynamics of strong fields. *Reports on Progress in Physics* **1977**, 40(3), 219.

Rhim, J. W.; Park, K. Self-similar occurrence of massless Dirac particles in Graphene under a magnetic field. *Physical Review B* **2012**, 86(23), 235411.

Schweppe, J.; Gruppe, A.; Bethge, K.; Bokemeyer, H.; Cowan, T.; Folger, H.; Greenberg, J. S.; Grein, H.; Ito, S.; Schule, R.; Schwalm, D.; Stiebing, K. E.; Trautmann, N.; Vincent, P.; Waldschmidt, M. Observation of a peak structure in positron spectra from U<sup>+</sup> Cm collisions. *Physical Review Letters* **1983**, 51(25), 2261.

Sengupta, R.; Bhattacharya, M.; Bandyopadhyay, S.; Bhowmick, A. K. A review on the mechanical and electrical properties of graphite and modified graphite reinforced polymer composites. *Progress in polymer science* **2011**, 36(5), 638-670.

Shen, J.; Zhu, Y.; Yang, X.; Li, C. Graphene quantum dots: emergent nanolights for bioimaging, sensors, catalysis and photovoltaic devices. *Chemical communications* **2012**, 48(31), 3686-3699.

Shytov, A.; Rudner, M.; Gu, N.; Katsnelson, M.; Levitov, L. Atomic collapse, Lorentz boosts, Klein scattering, and other quantum-relativistic phenomena in Graphene. *Solid state communications* **2009**, 149(27-28), 1087-1093.

Solin, S. A. The nature and structural properties of graphite intercalation compounds. *Adv. Chem. Phys* **1982**, 49, 455-532.

Su, F.-Y.; You, C.; He, Y. B.; Lv, W.; Cui, W.; Jin, F.; Li, B.; Yang, Q.-H.; Kang, F. Flexible and planar Graphene conductive additives for lithium-ion batteries. *Journal of Materials Chemistry* **2010**, 20(43), 9644-9650.

Wallace, P. R. The band theory of graphite. *Phys. Rev* **1947**. 71, 622–634.

Wang, G.; Shen, X.; Yao, J.; Park, J. Graphene nanosheets for enhanced lithium storage in lithium ion batteries. *Carbon* **2009**, 47(8), 2049-2053.

Wang, Y.; Wong, D.; Shytov, A. V.; Brar, V. W.; Choi, S.; Wu, Q.; Tsai, H.-Z.; Regan, W.; Zett, A.; Kawakami, R. K.; Louie, S. G.; Levitov L. S.; Crommie, M. F. Observing atomic collapse resonances in artificial nuclei on Graphene. *Science* **2013**, 340(6133), 734-737.

Yoo, E.; Kim, J.; Hosono, E.; Zhou, H. S.; Kudo, T.; Honma, I. Large reversible Li storage of Graphene nanosheet families for use in rechargeable lithium ion batteries. *Nano letters* **2008**, 8(8), 2277-2282.

Zheng, X. T.; Ananthanarayanan, A.; Luo, K. Q.; Chen, P. Glowing Graphene quantum dots and carbon dots: properties, syntheses, and biological applications. *Small* **2015**, 11(14), 1620-1636.